

1 **Supplemental Information for Chemical transport models often underestimate inorganic**
2 **atmospheric aerosol acidity in remote regions of the atmosphere**

3

4

5 Benjamin A. Nault, Pedro Campuzano-Jost, Douglas A. Day, Duseong S. Jo, Jason C. Schroder,
6 Hannah M. Allen, Roya Bahreini, Huisheng Bian, Donald R. Blake, Mian Chin, Simon L. Clegg,
7 Peter R. Colarco, John D. Crouse, Michael J. Cubison, Peter F. DeCarlo, Jack E. Dibb, Glenn S.
8 Diskin, Alma Hodzic, Weiwei Hu, Joseph M. Katich, Michelle J. Kim, John K. Kodros,
9 Agnieszka Kupc, Felipe D. Lopez-Hilfiker, Eloise A. Marais, Ann M. Middlebrook, J. Andrew
10 Neuman, John B. Nowak, Brett B. Palm, Fabien Paulot, Jeffrey R. Pierce, Gregory P. Schill, Eric
11 Scheuer, Joel A. Thornton, Kostas Tsigaridis, Paul O. Wennberg, Christina J. Williamson, and
12 Jose L. Jimenez

13

14 **Supplemental Information Section 1 - 6**

15 **Supplemental Information Tables S1 - S8**

16 **Supplemental Information Figures S1 - S31**

17 **S1 Constraints on Ammonia Mixing Ratio**

18 Ammonia is the most important atmospheric base, and plays a critical role in controlling
19 aerosol pH and ammonium balance¹, as discussed above. It also impacts new particle
20 formation^{2,3}. As discussed in Methods Section, even for campaigns missing ammonia
21 measurements, an important constraint can be placed from our thermodynamic analysis for the
22 potential mixing ratio of ammonia in the troposphere. For example, the point-to-point
23 comparison for the CalNex case study is noisy, but, on average, the modeled ammonia is within a
24 factor of 2 of the observed ammonia (Supplemental Figure 22 and 23). We expect this relative
25 uncertainty to potentially increase for regions of low ammonia concentrations (i.e., remote
26 locations) as most of the ammonia will be in the particle phase (Fig. 1c).

27 Generally, the estimated ammonia is low (<10 pptv) outside continental and biomass
28 burning-influenced air over the Pacific and Atlantic Ocean (Supplemental Figure 9). This is in
29 agreement with remote ammonia observations from satellites; though, the satellite detection
30 limits (3 - 5 pptv) are higher than the low mixing ratios reported in Supplemental Figure 9. These
31 low mixing ratios have two important implications. First, they further support low NH_x emissions
32 and mixing ratios over oceanic regions⁴ and that the lifetime of ammonia is short, preventing
33 high mixing ratios throughout the remote atmosphere. Second, the ternary nucleation rates by
34 sulfuric acid vapor, water vapor, and ammonia would be low, limiting new particle formation
35 from this pathway². The air masses with higher ammonia mixing ratios would have limited new
36 particle formation due to higher particle number concentration and condensational sink⁵. This is
37 in agreement with ammonia being unlikely to explain the observed new particle formation
38 observed over these oceanic basins during ATom-1 and -2⁵.

39 Over the continents (Supplemental Figure 9), there is high ammonia for regions affected
40 by agriculture and anthropogenic activities^{1,6}. In the upper troposphere and boreal forest, though,
41 in the absence of biomass burning plumes, there is minimal ammonia, further indicating (a)
42 boreal forests are a small source of ammonia⁶ and (b) although convection can transport
43 ammonia⁷, it is short-lived and the resulting mixing ratios are still low compared to the boundary
44 layer and lower free troposphere. Similar to over the oceans, the regions with higher ammonia
45 gas mixing ratios would have limited new particle formation due to the high aerosol mass
46 concentrations observed (Fig. 4).

47 The CTMs that include ammonia show relatively high biases both over the ocean basins
48 and over the continents (Supplemental Figure 9). Further, the models show orders of magnitude
49 higher ammonia in the free troposphere than what has been observed by satellite^{7,8} or other
50 remote sensing instruments⁹. This points to two important uncertainties in the CTMs: (a) high
51 biases in ammonia emissions from oceans⁴, as the oceanic boundary layer has 1 – 2 orders of
52 magnitude higher ammonia than the observationally-constrained ammonia value; and, (b) too
53 long of ammonia lifetime, as the concentrations remain high throughout the troposphere. Thus,
54 these two uncertainties are potentially driving the high bias in ammonium balance between
55 models and observations discussed throughout the manuscript and can impact the understanding
56 of new particle formation in the remote regions around the world.

57

58 **S2 Calculation of Hygroscopic Growth Factors**

59 The hygroscopic growth factors (HGF) were calculated to investigate how the inorganic
60 aerosol composition impacted water uptake and in turn diameter. This value has important

61 implications for direct radiative effect as ammonium-sulfate-like versus sulfuric-acid-like
62 aerosols have different values¹⁰. We estimated the HGF for every minute of flights for all
63 campaigns; then, we plotted and binned the calculated HGF data as a function of RH and NH_{4_Bal}.
64 To calculate the HGF, the total inorganic volume, measured by AMS (sulfate, nitrate, and
65 ammonium), was added to the volume from water, which was estimated by E-AIM:

$$66 \quad HGF = \left(\frac{volume_{water} + volume_{dry,aerosol}}{volume_{dry,aerosol}} \right)^{1/3} \quad \text{Eq. S1}$$

67 The dry aerosol volume was calculated by assuming a density of 1.78 g cm⁻³ for ammonium,
68 nitrate, and sulfate^{11,12}. Only inorganics were considered in Eq. S1 for consistency with the
69 GEOS-Chem DRE calculation, which assumes an external mixture of the aerosol components¹³.

70 The HGF, calculated from all the campaigns (Supplemental Table 2), were binned against
71 RH and NH_{4_Bal}. The dependence of HGF for T was smaller versus RH, as E-AIM operated with
72 the metastable assumption, making the aerosol liquid water more dependent on RH than T (and
73 thus not shown). The HGF shown in Supplemental Figure 6 for the CTMs was calculated by
74 using the average RH and NH_{4_Bal} to estimate the HGF from the look up table (Supplemental
75 Figure 5).

76

77 **S3 Theoretical E-AIM Calculation to Investigate Impact of RH and Aerosol Composition** 78 **on Ammonium Balance and pH**

79 Here, we describe a simple sensitivity study in the role of RH and aerosol composition on
80 aerosol pH. These sensitivity calculations were designed to study the large variation in relative
81 responses between NH_{4_Bal} and pH shown in Fig. 3. We adapted the theoretical model described
82 by Murphy et al.¹⁴. Similar to Murphy et al.¹⁴, total ammonium (NH_{3,g} + NH_{4⁺,p}) was kept

83 constant at 200 nmol m^{-3} , sulfate was varied between 5 to 1000 nmol m^{-3} , total nitrate ($\text{HNO}_{3,g} +$
84 $\text{NO}_{3,p}^-$) was kept constant at 0.01 nmol m^{-3} , and RH varied between 30 to 95%. We performed the
85 simulations for two temperatures, 298 and 243 K. The same E-AIM (Model IV) and definition of
86 pH was used here as throughout the paper. This is a significant difference compared to Murphy
87 et al.¹⁴, in that they used the pH definition based on the mole fraction of H^+ instead of molality of
88 H^+ . The results of the model are described in the main text.

89

90 **S4 Comparison of Volatile and Non-Volatile Volume Distribution, Description of** 91 **Condensational Sink Calculation, Description of Estimated Sea-Salt/Sodium and of Other** 92 **Cations, and Importance of Non-Volatile Cations**

93 Here, we investigate the importance of non-volatile cations (NVCs) in fine mode aerosol
94 and any potential impact NVCs may have on NH_{4_Bal} and pH. During ATom-1 and -2, the AMS
95 measured sea-salt in the marine boundary layer¹⁵, using the techniques described in Ovadnevaite
96 et al.¹⁶. However, this measurement does not provide information on whether the sea-salt was
97 internally or externally mixed with sulfate-organic dominated fine mode aerosol. The following
98 section investigates whether the sea-salt is internally or externally mixed into the fine aerosol and
99 any potential error in assuming sea-salt is externally mixed into the sulfate-organic dominated
100 fine mode aerosol. The summary of this section is that there are two main modes: (1) fine mode,
101 dominated by sulfate and organics, and minimal NVCs. Any NVCs are externally mixed, and
102 even if they were internally mixed, they would have minimal impact on NH_{4_Bal} and pH. (2) The
103 coarse mode, dominated by NVC, would subsequently have a different pH. The focus of the
104 paper is the fine mode aerosol..

105

106 **S4.1 Comparison of Volume Distributions**

107 Here we discuss comparisons of volatile versus non-volatile (refractory) volume
108 distributions measured during ATom, to investigate the mixing state of NVCs as well as their
109 importance to AMS measurements and condensation of acidic gases (e.g., sulfuric acid) in the
110 MBL. Condensing onto aerosol containing the NVCs would lead to the formation of non-volatile
111 salts, such as sodium sulfate or calcium sulfate, while condensing onto other aerosol would lead
112 to formation of ammonium salts or acidic aerosol (the focus of this study). During ATom-2, a set
113 of instruments, ultra-high-sensitivity aerosol size spectrometers (UHSAS), were used to
114 measure the size distribution of particles from 63 to 1000 nm (> 90% counting efficiency) and
115 the remaining aerosol number concentrations (i.e., aerosol containing non-volatile cations) after
116 heating the aerosol with a 300°C thermodenuder installed upstream with a residence time of 1.59
117 to 3.7 s, for the same diameter range^{17,18}. As shown in Supplemental Figure 13a and b, there are
118 two populations in the aerosol volume — between 100 to 400 nm diameter and > 600 nm
119 diameter. A much larger fraction of the non-volatile components are at larger sizes, suggesting a
120 high degree of external mixing of those components, similar to what Guo et al. suggested¹⁹. A
121 large fraction of the aerosol volume at > 600 nm is non-volatile, as it is measured by the denuded
122 instrument, which is outside the range of aerosol measured by the AMS²⁰. On the other hand, the
123 majority of the aerosol between 200 to 400 nm, the size range measured by the AMS and used
124 for the acidity calculations, is volatile. This is similar to what was observed by Murphy et al.²¹,
125 where they found most of the sea-salt volume occurs above 600 nm diameter. Finally, the volume
126 of refractory aerosol (e.g., sea-salt) in the size range of the AMS (Supplemental Figure 13) is

127 likely overestimated due to sea-salt being externally mixed^{22,23} and some fraction of the sizes
128 after denuding are smaller than in the atmosphere due to loss of some volatile material from
129 primary emissions²⁴.

130

131 **S4.2 Calculation of the Condensational Sink**

132 The condensational sink provided by the ambient aerosol is used for calculating the
133 condensational sink of sulfuric acid to determine whether it is internally or externally mixed with
134 sea-salt. The instruments used for this analysis are described above. The thermodenuder channel
135 measured non-volatile, refractory components of the aerosol, which includes sea-salt and black
136 carbon. The particle number size distributions of both UHSASs were used to calculate the
137 condensational sink for the total aerosol and the refractory aerosol. The calculations described in
138 Palm et al.²⁵ were used to estimate the condensational sink. Briefly, the condensational sink was
139 calculated with Eq. S2:

$$140 \quad CS = \int_0^{\infty} r\beta(r)N(r)dr \quad \text{Eq. S2}$$

141 where the integral is the first moment of the particle size distribution, r is the wet particle radius,
142 $N(r)$ is the particle number size distribution measured by either UHSAS, and

$$143 \quad \beta(r) = \frac{Kn+1}{0.377Kn+1 + \frac{4}{3}\alpha^{-1}Kn^2 + \frac{4}{3}\alpha^{-1}Kn} \quad \text{Eq. S3}$$

144 is the Fuchs-Sutugin correction²⁶. This corrects the mass transfer of the condensing gas (i.e.,
145 sulfuric acid) to the particle surface in the transition regime. α is the sticking coefficient of the
146 condensing species to the aerosol, which is assumed to be 1²⁷. $\beta(r)$ (Eq. S3) is a function of the
147 Knudsen number:

148 $Kn = \frac{\lambda_g}{r}$ Eq. S4

149 where λ_g is the mean free path of the condensing gas. Finally, a growth factor of 1 is assumed
150 here (no aerosol liquid water), which will be an underestimation of the condensational sink as
151 water will increase the radius of the aerosol. However, due to limited chemical information for
152 the aerosol composition < 100 nm and uncertainty on the amount of internal versus external
153 mixing for the particle size distribution measured in the refractory channel, the assumption of 1
154 provides the most robust comparison.

155

156 **S4.3 Comparison of Condensational Sink Distribution**

157 As the condensational sink is dependent on aerosol surface area and is also higher for
158 smaller particles in the free-molecular regime, it is weighed towards smaller diameters. This
159 means that the overall condensational sink is dominated by the volatile, non-denuded aerosol
160 (Supplemental Figure 13c and d) for diameters less than 600 nm, which is in the range of the
161 AMS detection. Thus, the condensation of sulfuric acid onto aerosol is expected to preferentially
162 occur onto aerosol containing non-volatile (refractory) aerosol, i.e., that observed by AMS.
163 Therefore, for models that calculate aerosol pH on-line with a thermodynamic model and input
164 all inorganic aerosol (sulfate, nitrate, ammonium, and submicron or accumulation mode sea-salt)
165 and assume the inorganic aerosol are all internally mixed appear to not reflect the real
166 atmosphere and lead to the higher aerosol pH, which would affect the predicted chemistry in
167 regions of high sea-salt (e.g., Fig. 1). Finally, similar to volume distribution, condensational sink
168 contributions of refractory aerosol (e.g., sea-salt) in the size range of the AMS (Supplemental
169 Figure 13) is likely overestimated due to sea-salt being externally mixed^{22,23} and some fraction of

170 the sizes after denuding are smaller than in the atmosphere due to loss of some volatile material
171 from primary emissions.

172

173 **S4.4 Description of Estimated Sea-Salt Volume/Mass Concentration Contribution**

174 The UHSAS with a thermal denuder inlet was used to measure refractory aerosol number
175 concentration and size. These data were used to estimate the integrated volume distribution of
176 refractory particles during ATom-2 (see above). Black carbon was measured during ATom-2 by a
177 single-particle soot photometer (SP2)²⁸. The measured mass concentration was converted to
178 volume concentration, assuming a density of 1.77 g cm⁻³ ²⁹. To estimate the sea-salt volume
179 concentration, it was assumed the refractory volume concentration was composed of black
180 carbon and sea-salt; thus, the sea-salt volume concentration was determined by difference
181 between the refractory and black carbon volume. Then, the sodium mass concentration
182 (Supplemental Figure 14) was estimated by assuming a sea-salt density of 1.45 g cm⁻³ ³⁰ and
183 assuming the chemical composition of sea-salt was approximately sodium chloride (NaCl).

184

185 **S4.5 Importance of Non-Volatile Cations for PM₁**

186 An important question is whether NVCs, including sodium (Na⁺) from sea-salt, are
187 internally mixed and thus should be included in calculating both pH and NH₄_{Bal}. In past studies,
188 the inclusion of these NVCs was shown to mainly be important for aerosols larger than the AMS
189 size range^{19,20}. In this study, we focus on the pH of non-sea-salt-sulfate (NSS); the pH of sea-salt
190 aerosols will be higher and is not analyzed here. Multiple pieces of evidence support the
191 exclusion of sea-salt from the pH calculations of NSS sulfate: 1) the fraction of submicron Na⁺

192 and sea-salt in the AMS size range is small, and even if it all was internally mixed with NSS
193 sulfate, it would not perturb NH_{4_Bal} or pH much (NH_{4_Bal} by <1% and pH by 0.1 units, at most)
194 due to the low Na^+ mass concentration (mean = $0.01 \mu\text{g sm}^{-3}$) (Supplemental Figure 13 and
195 Supplemental Figure 14); 2) sea-salt and NSS sulfate are externally mixed, due to (a) separate
196 emission pathways for NSS sulfate³¹ and NH_x^4 versus sea-salt³² and to (b) sulfuric acid formed in
197 the MBL condensing on the dominant condensational sink of NSS sulfate, and not on the sea-salt
198 particles. Thus, for NSS sulfate²⁰, sea-salt should not be included for pH estimations. This leads
199 to lower pH than estimated by models that include accumulation-mode sea-salt in the pH
200 calculations (GEOS-Chem v10 and v12). Finally, as discussed in SI Sect. 4.6 (Supplemental
201 Figure 15), the influence of other NVCs (such as K^+ and $\text{Ca}^{2.+}$) on NH_{4_Bal} and pH is minimal,
202 like Na^+ ; thus, for aerosols in the AMS size range, NVCs in general do not impact the
203 conclusions discussed here.

204 In order to explore the large differences between models and observations in the BL, we
205 look specifically at two recent versions of the GEOS-Chem model (v10 and v12). Above the BL,
206 these two models capture both the trend (Supplemental Table 6) and probability distribution
207 function (Supplemental Figure 12) of pH. GEOS-Chem, by default, includes accumulation mode
208 sea-salt in the calculation of aerosol pH³³. The short lifetime of sea-salt in GEOS-Chem³⁴
209 minimizes the vertical mixing of sea-salt into the free and upper troposphere, in line with the
210 observations from Murphy et al.²¹. Therefore, the lack of sea-salt leads to better agreement
211 between observations and GEOS-Chem above the BL; whereas, in the BL, the inclusion of
212 sea-salt leads to the positive bias in the submicron aerosol pH (Fig. 3 and Supplemental Figure
213 12).

214

215 **S4.6 Minimal Influence from Other Non-Volatile Cations**

216 Besides sea-salt, other sources of NVCs include dust¹⁹ and biomass burning³⁵. Dust was
217 rarely observed for particles smaller than 1 μm ³⁶, except on one flight during ATom-1, where
218 Saharan dust outflow was directly sampled. As discussed in Guo et al.²⁰, dust accounted for ~1%
219 of PM_{10} volume during ATom, meaning NVCs from dust generally would not impact the overall
220 NH_4_{Bal} and pH calculated from observations. Potassium accounts for the majority of the NVC
221 mass concentration for PM_{10} from biomass burning^{35,37}; however, as shown in Supplemental
222 Figure 15, the median potassium concentration observed during campaigns focused on biomass
223 burning (ARCTAS-B and SEAC⁴RS) was $< 0.10 \mu\text{g sm}^{-3}$ and for the ATom campaigns, $\sim 0 \mu\text{g}$
224 sm^{-3} . This represents $< 5\%$ difference in NH_4_{Bal} and < 0.02 pH unit difference. Thus, for this
225 study and the size-range of aerosol observed by the AMS, NVCs generally do not affect the
226 NH_4_{Bal} and pH reported here.

227

228 **S4.7 Minimal Partitioning of Ammonia to Sea-Salt (and Other Less Acidic Aerosol)**

229 Another important aspect of sea-salt and other aerosols impacted by NVCs is that the pH
230 is increased, which leads to lower partitioning of ammonia to the particle-phase³⁸. Prior studies
231 have observed that the pH for aerosol strongly impacted by sea-salt is > 2 ³⁹⁻⁴², which generally
232 leads to $> 90\%$ of total NH_x (gas + particle) partitioning to the gas-phase³⁸. Note, this aerosol is
233 also mainly coarse aerosol. This has been further verified in that the aerosol with high sea-salt
234 and high pH has minimal ammonium content⁴⁰⁻⁴². Thus, it is expected that neglecting ammonium
235 uptake for sea-salt aerosols will not bias the results described here.

236

237 **S5 Sensitivity to Organic Contribution to Inorganic Mass Concentration**

238 As the nominally inorganic ions measured by the AMS can in principle be produced from
239 both inorganic and organic compounds in aerosol⁴³⁻⁴⁶, a sensitivity analysis for each aerosol
240 species reported from the AMS was conducted for its impacts on aerosol pH and $\text{NH}_4\text{-Bal}$.

241

242 **S5.1 Potential Interference of Organic Oxidized Nitrogen Compounds on Nitrate**

243 Organic oxidized nitrogen in aerosol are thought to be mainly organic nitrates (pRONO_2)
244 outside biomass burning plumes^{44,47,48}, but can also include nitroaromatics⁴⁹ in biomass burning⁵⁰.
245 These species thermally decompose and fragment mainly into NO^+ and NO_2^+ ions, leading to a
246 characteristic NO_x^+ ratio that is different than inorganic nitrate^{43,44}. However, some of the
247 campaigns used here did not perform this analysis, and for consistency we use the total reported
248 nitrate as inorganic nitrate. Thus, the potential influence of this interference on the total nitrate is
249 investigated.

250 Aerosol pH was calculated with the aerosol nitrate corrected for pRONO_2 for the
251 SEAC⁴RS campaign, as this had a mixture of inorganic nitrate from biomass burning^{51,52} and
252 pRONO_2 from biogenic gas-phase chemistry⁵³. The change in pH by removing pRONO_2 from
253 the nitrate mass concentration, in general, is minimal, with a few point-to-point changes
254 (Supplemental Figure 29). This is in agreement with the comparison of aerosol pH shown in
255 Supplemental Figure 21, where there is minimal impact on the predicted aerosol pH upon using
256 either AMS + CIMS total nitrate (particle nitrate, which includes pRONO_2 , and HNO_3) or MC/IC
257 total nitrate (particle nitrate, which should include minimal pRONO_2 , and HNO_3). Though

258 hydrolysis of pRONO₂ is a potentially important sink that forms an alcohol and HNO₃ and a
259 potential interference for MC/IC, most hydrolysis rates should be rapid enough to occur in the
260 aerosol phase prior to sampling with the MC/IC⁵⁴. Thus, it is not expected that pRONO₂ will
261 substantially affect the total nitrate observed by the MC/IC. Therefore, it is not expected that
262 inclusion of pRONO₂ has a large impact on the predicted pH, as over continental, polluted
263 regions, most of the total nitrate is inorganic⁵⁵; whereas, over clean, remote regions (i.e., ATom),
264 nitrate composes a small fraction of the total inorganic mass concentration³⁶ and thus plays a
265 small role in the thermodynamic calculations of aerosol and aerosol pH.

266

267 **S5.2 Potential Interference of Organic Reduced Nitrogen Compounds on Ammonium**

268 Organic reduced nitrogen compounds in aerosol, such as amines and pyridine, have been
269 shown to contribute to charge balancing of sulfuric acid, especially for new particle formation
270 events⁵⁶. Further, amines have been suggested to potentially appear as total ammonium in the
271 AMS due to thermal decomposition and ionization⁴⁵. The influence of the organic reduced
272 nitrogen compounds to ammonium balance and aerosol pH are investigated here.

273 Various organic reduced nitrogen compounds have been investigated in the AMS and
274 compared against the NIST reference spectra⁵⁷. It was found that the AMS spectra generally
275 agreed with the NIST spectra. That means for cyclic organic reduced nitrogen compounds, such
276 as pyridine, there is no contribution to the ammonium signal (NH⁺, NH₂⁺, NH₃⁺)⁵⁸. For amines, it
277 is expected <2% of the total signal will be observed as ammonium signal⁵⁹. Further, Ge et al.⁵⁷
278 observed that the majority of the amine signal between *m/z* 14 and 18 was due to H_xO_y⁺ ions and
279 not NH_x⁺ ions. Thus, at the typical mass concentrations observed at the marine surface and

280 marine boundary layer (Supplemental Table 8), it is expected that, at most, 0.6 ng sm^{-3}
281 ammonium would be observed due to oceanic amines. This is less than 2% of the observed
282 average ammonium in the marine boundary layer during ATom-1 and -2 (42 and 49 ng sm^{-3} ,
283 respectively³⁶). Thus, the amines have minimal impact on the measurement of ammonium
284 balance in the marine boundary layer. It has been observed that the amines rapidly decrease with
285 altitude⁶⁰, similar to methane sulfonic acid⁶¹, with which amines are correlated⁶⁰. Therefore,
286 amines are expected to have an even smaller effect on ammonium balance outside the marine
287 boundary layer (where ammonium concentrations were similar).

288 A more important way that the organic reduced nitrogen compounds could affect the
289 results reported here is by acting as a base for the sulfuric acid. As shown in Supplemental Table
290 8 and Supplemental Figure 31, the estimated organic reduced nitrogen compounds account for a
291 small fraction of the ammonium mass concentration ($\leq 10\%$ for amines and on average, $< 0.1\%$
292 for pyridine). A sensitivity analysis was conducted, where it was assumed that the organic
293 reduced nitrogen compounds behaved like ammonium, and the ammonium mass concentration
294 was increased by 10% throughout ATom-2 (Supplemental Figure 30). Similar to the sensitivity
295 analysis for pRONO_2 , there is point-to-point variability in the predicted pH by increasing
296 ammonium for potential organic reduced nitrogen compounds; however, the slope and average
297 pH increase by a small amount (15% for slope and ~ 0.06 pH units for the average). Considering
298 the best estimated uncertainty in pH is ~ 0.5 pH units^{62,63}, the majority of the data falls within this
299 uncertainty (Supplemental Figure 30). Further, an upper estimate for organic reduced nitrogen
300 compounds for all ammonium was considered, which should not be the case above the boundary
301 layer⁶⁰, leading to an upper limit change in the predicted changes in aerosol pH. Thus, is it

302 expected that neglecting reduced nitrogen organic compounds will significantly impact the
303 predicted pH reported here.

304

305 **S5.3 Potential Interference of Organosulfates on Sulfate**

306 Organosulfates have been shown to thermally decompose and ionize into various SO_x
307 ions (i.e., SO^+ , SO_2^+ , SO_3^+ , HSO_3^+ , and H_2SO_4^+), impacting the total sulfate mass concentration⁴⁶.
308 In biogenic regions, the organosulfates may contribute a substantial fraction of the total sulfate
309 mass concentration⁶⁴. However, deconvolving the total sulfate signal into organic versus
310 inorganic sulfate is difficult due to various matrix effects^{46,65}, making correction for this signal
311 challenging. Though the fractional contribution of organosulfates to ground level total sulfate can
312 be high occasionally at ground sites ($>10\%$)⁶⁴, it has generally been found to be much lower for
313 airborne observations ($<7\%$)⁶⁶. For example, during ATom, 1% or less of the sulfate was
314 organosulfate, calculated from PALMS organosulfate and AMS sulfate mass concentrations,
315 which would lead to a small change in the average sulfate mass concentration and thus to
316 ammonium balance. Further, as described in Riva et al.⁶⁴, the majority of the campaigns used in
317 this study are in locations with low epoxide to inorganic sulfate ratios, leading to minimal
318 conversion of inorganic sulfate to organosulfate. Therefore, organosulfates are not expected to
319 affect the reported ammonium balance and aerosol pH reported here.

320

321 **S6 Comparison of Measured and E-AIM Modeled Volatile Species**

322 Since accurate partitioning between gas-phase nitric acid and particle-phase nitrate
323 indicates that the model predictions are reasonably accurate and hence the calculated aerosol pH
324 is accurate to within ± 0.5 pH^{62,67} units (Fig. 1c), the model output was compared against

325 observations for all campaigns (Supplemental Figure 18 and 19). We found that for all but two
326 campaigns (INTEX-B and ATom-2), the predicted versus observed gas-phase nitric acid and
327 aerosol-phase nitrate were typically within the instrumental uncertainty of the observations
328 (Supplemental Figure 20). For ATom-2, the total nitrate was low and near the AMS
329 limit-of-detection³⁶. From Fig. 1c, this would suggest extremely acidic aerosol, which is what is
330 calculated by the model (Fig. 3 and Fig. 4). Thus, the low nitrate mass concentration is difficult
331 to compare against the E-AIM model predictions, as this is near the noise of the measurement.
332 The results presented are statistically similar (t-test) with and without INTEX-B and ATom-2.

333 As mentioned above, some campaigns had two measurements of total nitrate through
334 CF_3O^- CIMS (HNO_3) plus AMS (NO_3) or MC/IC (HNO_3 plus NO_3^-), and for some campaigns,
335 there were large disagreements for some subsets of the data between these two total nitrate
336 measurements. However, as shown in Supplemental Figure 18, this disagreement does not
337 substantially affect the aerosol pH, with slope differences of less than 2%. Though for some
338 campaigns the evaluation plots of gas- and particle-phase nitrate is worse using the MC/IC
339 compared to the CIMS and AMS and led to increased scatter in the aerosol pH (Supplemental
340 Figure 21), it did not impact the average aerosol pH.

341 CalNex was the only campaign with gas-phase ammonia measurements. This campaign
342 was used to investigate potential biases using the iteration method for ammonia gas for the other
343 10 campaigns that did not have ammonia measurements. We ran E-AIM similar to other
344 campaigns (without ammonia gas mixing ratios as input) and with total NH_x (ammonia gas plus
345 particle-phase NH_4) (Supplemental Figure 22). In the E-AIM model without ammonia gas input,
346 there is a larger point-to-point scatter for the predicted versus observed ammonia; however, the

347 model predicted the campaign average ammonia gas-phase concentration within a factor of 2
348 (Supplemental Figure 22 and 23). On the other hand, the model, on average, predicted the
349 partitioning of the gas- versus particle-phase ammonia and the predicted particle-phase
350 ammonium well (Supplemental Figure 22). Finally, the predicted pH changed by ~0.1 pH unit
351 between the model with and without total ammonia input (Supplemental Figure 24a). The
352 regression between the two cases shows some point-to-point variability ($R^2 = 0.78$) but still
353 shows a slope near 1 (1.11) (Supplemental Figure 24b). Therefore, these sensitivity analyses
354 suggest that the predicted aerosol pH for the campaigns without ammonia gas-phase
355 measurements are well constrained by the use of total nitrate, similar to prior studies⁶⁸.

356 **Supplemental Tables**

357

358 *Supplemental Table 1. References for processes represented in Fig. 1.*

Process	Reference
IEPOX Reaction Probability	Gaston et al. ⁶⁹
HO ₂ Reaction Probability	Thornton et al. ⁷⁰
Iron pH dependent dissolution	Meskhidze et al. ⁷¹
S(IV) Compound and Aqueous Oxidation	Seinfeld and Pandis ²⁷
Partitioning NH ₃ /NH ₄ ⁺ , HNO ₃ /NO ₃ ⁻ , HCl/Cl ⁻	Guo et al. ³⁸
Aldehyde/Diol Equilibrium (Brown Carbon)	Ackendorf et al. ⁷²
Organic aerosol phase separation	Losey et al. ⁷³

359

360 *Supplemental Table 2. Campaigns and subregions used in this study.*

Location	Field Campaign	Coordinates		Time Period	Season
		Longitude (°)	Latitude (°)		
Central Mexico	MILAGRO ⁷⁴	-102 – -88	16 – 28	04 March 2006 – 29 March 2006	Spring
Western US & Eastern Pacific	INTEX-B ⁷⁵	-141 – -118	37 - 54	17 April 2006 – 15 May 2006	Spring
Canada, Alaska, Greenland	ARCTAS-A ⁷⁶	-180 – -37	60 - 90	18 March 2008 – 19 April 2008	Spring
Canada, Greenland	ARCTAS-B ⁷⁶	-136 – -37	50 – 87	26 June 2008 – 13 July 2008	Summer
California, USA	CalNex ⁷⁷	-124 – -115	33 – 40	20 April 2010 – 22 June 2010	Spring
Central and Eastern USA	DC3 ⁷⁸	-106 – -78	30 – 43	04 May 2012 – 23 June 2012	Spring
USA	SEAC ^{4RS} ⁷⁹	-126 – -79	19 – 51	02 August 2013 – 23 Sept 2013	Summer
Eastern USA	WINTER ^{68,80}	-85 – -67	32 – 43	01 Feb 2015 – 15 March 2015	Winter
South Korea	KORUS-AQ ^{55,81}	123 – 133	30 – 39	01 May 2016 – 09 June 2016	Spring
ATom >50°	ATom-1 & -2 ³⁶	-150 – 0	>50	29 July 2016 – 23 August 2016; 26 Jan 2017 – 21 Feb 2016	Summer ^a Winter ^b
ATom Pacific 25° - 50°	ATom-1 & -2 ³⁶	-180 – -130	25 – 50	29 July 2016 – 23 August 2016; 26 Jan 2017 – 21 Feb 2016	Summer ^a Winter ^b
ATom Pacific -25° to 25°	ATom-1 & -2 ³⁶	-180 – -130	-25 – 25	29 July 2016 – 23 August 2016; 26 Jan 2017 – 21 Feb 2016	Summer ^a Winter ^b
ATom Pacific -50° to -25°	ATom-1 & -2 ³⁶	-180 – -130	-50 – -25	29 July 2016 – 23 August 2016; 26 Jan 2017 – 21 Feb 2016	Summer ^a Winter ^b
ATom <-50°	ATom-1 & -2 ³⁶	-180 – -30	< -50	29 July 2016 – 23 August 2016; 26 Jan 2017 – 21 Feb 2016	Summer ^a Winter ^b
ATom Atlantic -50° to -25°	ATom-1 & -2 ³⁶	-45 – 0	-50 – -25	29 July 2016 – 23 August 2016; 26 Jan 2017 – 21 Feb 2016	Summer ^a Winter ^b
ATom Atlantic -25° to 25°	ATom-1 & -2 ³⁶	-45 – 0	-25 – 25	29 July 2016 – 23 August 2016; 26 Jan 2017 – 21 Feb 2016	Summer ^a Winter ^b
ATom Atlantic 25° - 50°	ATom-1 & -2 ³⁶	-45 – 0	25 – 50	29 July 2016 – 23 August 2016; 26 Jan 2017 – 21 Feb 2016	Summer ^a Winter ^b

361

362 ^aATom-1 was during boreal summer

363 ^bATom-2 was during boreal winter

364 *Supplemental Table 3. Instruments used in this study.*

Campaign	NO₃ Measurement	SO₄ and NH₄ Measurement	NH₃ Measurement	HNO₃ Measurement
MILAGRO	HR-AMS ^{82,83}	HR-AMS ^{82,83}	N/A	CF ₃ O-CIMS ⁸⁴
INTEX-B	HR-AMS ^{82,85}	HR-AMS ^{82,85}	N/A	CF ₃ O-CIMS ⁸⁴
ARCTAS-A	HR-AMS ^{82,86} MC/IC ⁸⁷	HR-AMS ^{82,86}	N/A	CF ₃ O-CIMS ⁸⁴ MC/IC ⁸⁷
ARCTAS-B	HR-AMS ^{82,86} MC/IC ⁸⁷	HR-AMS ^{82,86}	N/A	CF ₃ O-CIMS ⁸⁴ MC/IC ⁸⁷
CalNex	c-ToF-AMS ^{88,89}	c-ToF-AMS ^{88,89}	Acetone-CIMS ⁹⁰	SiF ₅ ⁻ -CIMS ⁹¹
DC3	HR-AMS ⁸² MC/IC ⁸⁷	HR-AMS ⁸²	N/A	CF ₃ O-CIMS ⁸⁴ MC/IC ⁸⁷
SEAC ⁴ RS	HR-AMS ⁸² MC/IC ⁸⁷	HR-AMS ⁸²	N/A	CF ₃ O-CIMS ⁸⁴ MC/IC ⁸⁷
WINTER	HR-AMS ^{80,82}	HR-AMS ^{80,82}	N/A	I-CIMS ⁹²
KORUS-AQ	HR-AMS ^{55,82} MC/IC ⁸⁷	HR-AMS ^{55,82}	N/A	CF ₃ O-CIMS ⁸⁴ MC/IC ⁸⁷
ATom-1	HR-AMS ^{20,36,82} MC/IC ⁸⁷	HR-AMS ^{20,36,82}	N/A	CF ₃ O-CIMS ⁸⁴ MC/IC ⁸⁷
ATom-2	HR-AMS ^{20,36,82} MC/IC ⁸⁷	HR-AMS ^{20,36,82}	N/A	CF ₃ O-CIMS ⁸⁴ MC/IC ⁸⁷

365

366 *Supplemental Table 4. Chemical transport models used along with brief information about the*
 367 *models (model year, output, etc.). For models that calculated pH on-line, ISORROPIA v2 was*
 368 *used.*

Model	AeroCom-II or Post-AeroCom-II	pH Calculated on-line/off-line	Model Year	Reference
CCSM4	AeroCom-II	off-line	01/2006 - 12/2006	Tsigaridis et al. ⁹³
GISS-MATRIX	AeroCom-II	off-line	01/2006 - 12/2006	Tsigaridis et al. ⁹³
GISS-ModelE	AeroCom-II	off-line	01/2006 - 12/2006	Tsigaridis et al. ⁹³
TM4-ECPL-F	AeroCom-II	N/A	01/2006 - 12/2006	Tsigaridis et al. ⁹³
GEOS-Chem v10	Post-AeroCom-II	on-line	08/2013 - 07/2014	Marais et al. ⁹⁴
GEOS-Chem v12	Post-AeroCom-II	on-line	07/2013 - 06/2014	Jo et al. ⁹⁵
GEOS-5	Post-AeroCom-II	off-line	03/2016 - 02/2017	Bian et al. ⁹⁶
GEOS-Chem TOMAS	Post-AeroCom-II	off-line	01/2016 - 12/2016	Kodros and Pierce ⁹⁷
AM4.1	Post-AeroCom-II	on-line	01/2007 - 12/2007	Horowitz et al. ⁹⁸

369

370 *Supplemental Table 5. Slopes and intercepts for ammonium balance*
 371 *$((NH_4/18)/((2 \times SO_4/96) + (NO_3/62)))$ versus $\log_{10}(Inorganic PM_{10})$ for observations and models by*
 372 *pressure levels.*

Data	Pressure Level	Slope	Intercept	R ²
Ambient Observations	Surface to 800 hPa	0.37±0.07 ^a	0.60±0.05 ^c	0.57
	800 to 400 hPa	0.53±0.07 ^a	0.76±0.04 ^c	0.74
	400 to 250 hPa	0.45±0.07 ^a	0.57±0.07 ^c	0.66
CCSM4	Surface to 800 hPa	-0.04±0.09	0.86±0.05	0.01
	800 to 400 hPa	-0.20±0.20	0.83±0.16	0.04
	400 to 250 hPa	0.46±0.28	1.49±0.40	0.10
GISS-MATRIX	Surface to 800 hPa	-0.08±0.11	0.65±0.05	0.02
	800 to 400 hPa	0.27±0.15 ^b	0.79±0.11 ^d	0.12
	400 to 250 hPa	0.83±0.15 ^b	1.58±0.20	0.59
GISS-ModelE	Surface to 800 hPa	0.08±0.12	0.90±0.06	0.02
	800 to 400 hPa	0.60±0.20 ^b	1.24±0.14	0.29
	400 to 250 hPa	1.26±0.25	2.27±0.31	0.54
TM4-ECPL-F	Surface to 800 hPa	0.40±0.05 ^b	0.84±0.04	0.70
	800 to 400 hPa	0.35±0.11 ^b	1.06±0.12	0.32
	400 to 250 hPa	0.84±0.14	1.54±0.22	0.59
GEOS-Chem v10	Surface to 800 hPa	0.31±0.08 ^b	0.73±0.04	0.40
	800 to 400 hPa	0.36±0.13 ^b	0.79±0.08 ^d	0.25
	400 to 250 hPa	0.18±0.16 ^b	0.60±0.13	0.06
GEOS-Chem v12, Default	Surface to 800 hPa	0.42±0.08 ^b	0.57±0.04 ^d	0.52
	800 to 400 hPa	0.43±0.10 ^b	0.66±0.05 ^d	0.44
	400 to 250 hPa	0.46±0.11 ^b	0.64±0.07 ^d	0.43
GEOS-Chem TOMAS	Surface to 800 hPa	0.23±0.09 ^b	0.71±0.04 ^d	0.22
	800 to 400 hPa	0.28±0.12 ^b	0.69±0.07 ^d	0.19
	400 to 250 hPa	0.31±0.12 ^b	0.65±0.08 ^d	0.22
GEOS-5	Surface to 800 hPa	0.10±0.07	0.48±0.03	0.10
	800 to 400 hPa	0.35±0.09 ^b	0.66±0.07 ^d	0.41
	400 to 250 hPa	0.63±0.12 ^b	1.02±0.11	0.57
AM4.1	Surface to 800 hPa	0.28±0.07 ^b	0.59±0.03 ^d	0.41
	800 to 400 hPa	0.46±0.10 ^b	0.75±0.04 ^d	0.48
	400 to 250 hPa	0.65±0.09 ^b	0.97±0.07	0.68

374 ^aThe observational trends at all three pressure levels are statistically similar at 95% confidence interval.

375 ^bThe trend in model is statistically similar to the trend in observation at 95% confidence interval.

376 ^cThe observational y-intercept at all three pressure levels are statistically similar at 95% confidence
 377 interval.

378 ^dThe y-intercept from model results is statistically similar to the y-intercept from the observations at 95%
 379 confidence interval. Only compared with slopes that were statistically similar (^b).

380 ^e The y-intercept from model results is statistically similar to the y-intercept from the observations at
 381 97.5% confidence interval. Only compared with slopes that were statistically similar (^b).

382 *Supplemental Table 6. Slopes and intercepts for aerosol pH versus log₁₀(Inorganic PM₁) for*
 383 *observations and models by pressure levels. For TM4-ECPL-F, there are not enough outputs to*
 384 *calculate aerosol pH.*

Data	Pressure Level	Slope	Intercept	R ²
Ambient Observations	Surface to 800 hPa	0.97±0.18 ^a	0.36±0.12 ^c	0.55
	800 to 400 hPa	1.38±0.15 ^a	0.60±0.11 ^c	0.64
	400 to 250 hPa	1.35±0.24 ^a	0.54±0.21 ^c	0.72
CCSM4	Surface to 800 hPa	0.00±0.16	0.63±0.09	0.00
	800 to 400 hPa	-0.33±0.26	1.51±0.18	0.08
	400 to 250 hPa	-0.58±0.19	1.56±0.25	0.34
GISS-MATRIX	Surface to 800 hPa	0.35±0.38 ^b	0.69±0.15 ^d	0.04
	800 to 400 hPa	0.52±0.39 ^b	1.30±0.28	0.09
	400 to 250 hPa	1.45±0.43 ^b	2.32±0.58	0.38
GISS-ModelE	Surface to 800 hPa	0.07±0.23	1.68±0.11	0.00
	800 to 400 hPa	1.52±0.63 ^b	3.39±0.47	0.20
	400 to 250 hPa	2.08±0.76	4.12±0.95	0.24
TM4-ECPL-F	Surface to 800 hPa	–	–	–
	800 to 400 hPa	–	–	–
	400 to 250 hPa	–	–	–
385 GEOS-Chem v10	Surface to 800 hPa	-0.72±0.36	1.70±0.17	0.15
	800 to 400 hPa	0.90±0.69 ^b	1.01±0.43 ^d	0.07
	400 to 250 hPa	3.03±0.90	2.52±0.75	0.33
GEOS-Chem v12, Default	Surface to 800 hPa	-0.39±0.31	1.16±0.14	0.06
	800 to 400 hPa	0.67±0.36 ^b	0.14±0.16	0.13
	400 to 250 hPa	1.44±0.32 ^b	0.30±0.20	0.48
GEOS-Chem TOMAS	Surface to 800 hPa	0.96±0.26 ^b	0.58±0.12 ^d	0.37
	800 to 400 hPa	1.08±0.37 ^b	0.67±0.22 ^d	0.28
	400 to 250 hPa	1.41±0.36 ^b	0.74±0.23 ^d	0.40
GEOS-5	Surface to 800 hPa	0.90±0.22 ^b	0.49±0.11 ^d	0.42
	800 to 400 hPa	1.68±0.24 ^b	1.47±0.19	0.68
	400 to 250 hPa	1.61±0.49 ^b	1.64±0.48	0.32
AM4.1	Surface to 800 hPa	0.84±0.19 ^b	0.13±0.09 ^d	0.45
	800 to 400 hPa	1.63±0.29 ^b	0.44±0.12 ^d	0.58
	400 to 250 hPa	2.06±0.33	0.84±0.23	0.63

386 ^aThe observational trends at all three pressure levels are statistically similar at 95% confidence interval.

387 ^bThe trend in model is statistically similar to the trend in observation at 95% confidence interval.

388 ^cThe observational y-intercept at all three pressure levels are statistically similar at 95% confidence
 389 interval.

390 ^dThe y-intercept from model results is statistically similar to the y-intercept from the observations at 95%
 391 confidence interval. Only compared with slopes that were statistically similar (^b).

392 *Supplemental Table 7. Description of GEOS-Chem v12 sensitivity runs conducted for Fig. 7.*

Model	Inorganic Phase State Considered	Oceanic NH_x Emissions	Reduced/Increased NH₃ Henry's Constant	Reduced Terrestrial NH₃ Emissions
Base	No	GEIA	N/A	No
Update HGF	Yes	GEIA	N/A	No
Update HGF and Decreased NH _x H	Yes	GEIA	Reduced	No
Update HGF Reduced NH _x Ocean Emiss.	Yes	Paulot et al. ⁴	N/A	No
Update HGF Reduced NH _x Ocean & Cont. Emiss.	Yes	Paulot et al. ⁴	N/A	Yes
Update HGF Reduced NH _x Emissions and Increased NH _x H	Yes	Paulot et al. ⁴	Increased	No

393

394 *Supplemental Table 8. Evaluation of reduced nitrogen organic compounds in aerosol from*
 395 *different studies. Unless otherwise noted, the values reported are the mean from the study.*

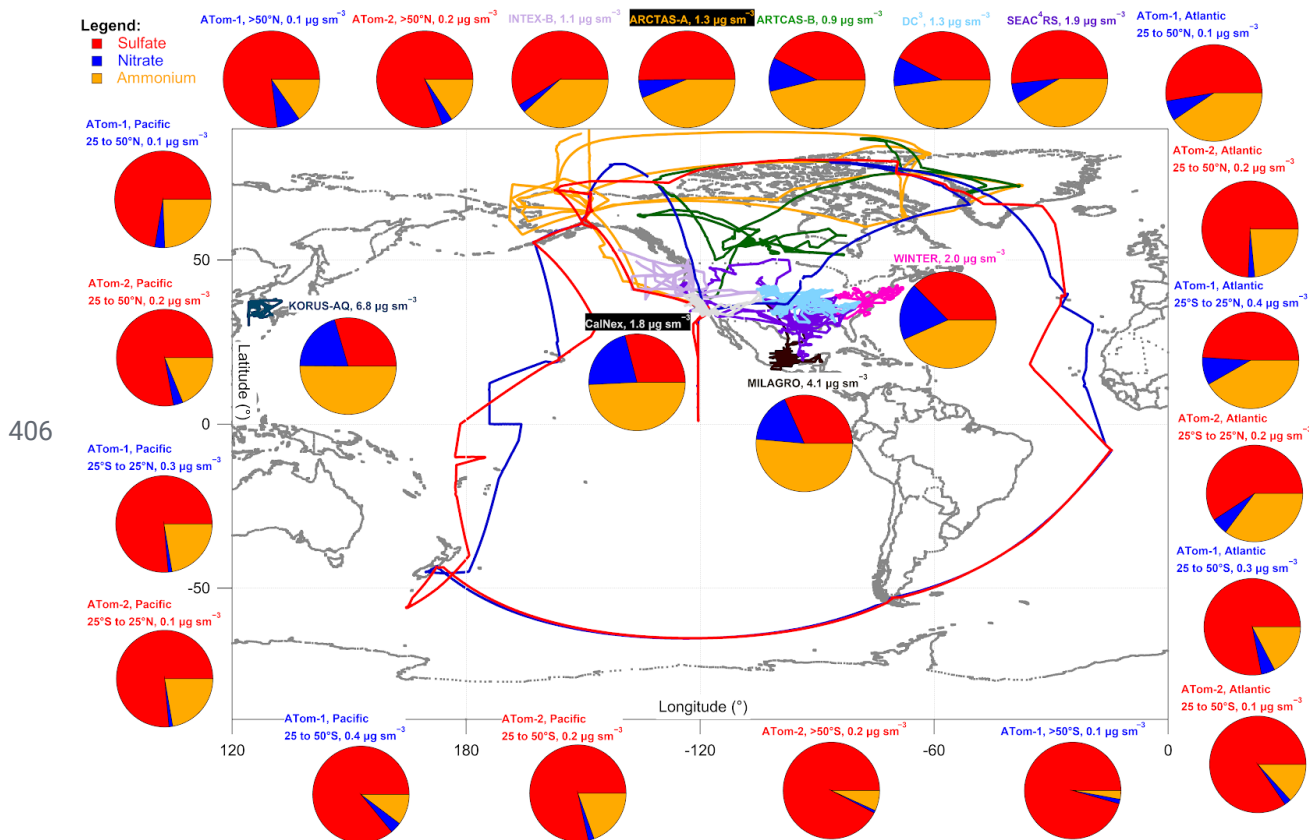
Reference	Amines (ng m ⁻³)	Ammonium (ng m ⁻³)	Amines: Ammonium ^a	Location	Dates Sampled
Müller et al. ⁹⁹	Mean = 0.57 Median = 0.53	Mean = 80 Median = 63	Mean = 0.007 Median = 0.008	16.86°N, 24.87°W & 17.59°N, 24.28°W	May 2007 - June 2008
van Pinxteren et al. ¹⁰⁰	13	690	0.02	16°N, 24°W to 5°S, 4°E	22 June - 21 July, 2011
Frossard et al. ¹⁰¹	30	N/A	N/A	See Ref. 132; overview of multiple studies	See Ref. 132; overview of multiple studies
Sorooshian et al. ⁶⁰	22	N/A	N/A	37.0°N, 123.5°W to 35.5°N, 122.0°W & 38.10°N, 122.96°W	June 2005 - July 2007
Youn et al. ¹⁰²	14	240	0.06	32.23°N, 110.95°W	July 2012 - June 2013
Gibb et al. ¹⁰³	5	44	0.11	20°N, 57°E to 7°N, 67°E	August - December 1994
Facchini et al. ¹⁰⁴	8	N/A	N/A	53°N, 10°W	11 June - 6 July, 2006
Huang et al. ^{105,b}	Mean = 11 Median = 7	Mean = 190 Median = 140	Mean = 0.06 Median = 0.05	53.55°N, 8.58°E to 33.92°S, 18.42°E or 53.17°N, 70.93°W	April 2011 - November 2012

396 ^aThe ratio is mass concentration ratio, as the amines are a mixture of compounds. Thus, the ratio
 397 should be smaller for the molar ratio, once the amines are converted to equivalent ammonium
 398 molar concentration.

399 ^bAerosol amines were measured by an Aerosol Mass Spectrometer. A large fraction of the
400 aerosol identified as marine nitrogen-containing OA was assigned to non-nitrogen-containing
401 fragments (82%, with a large oxygen content) versus nitrogen-containing fragments (18%).
402 Therefore, the amines mass concentration was determined by multiplying the entire marine
403 nitrogen-containing OA by the nitrogen fragment fraction of the OA.

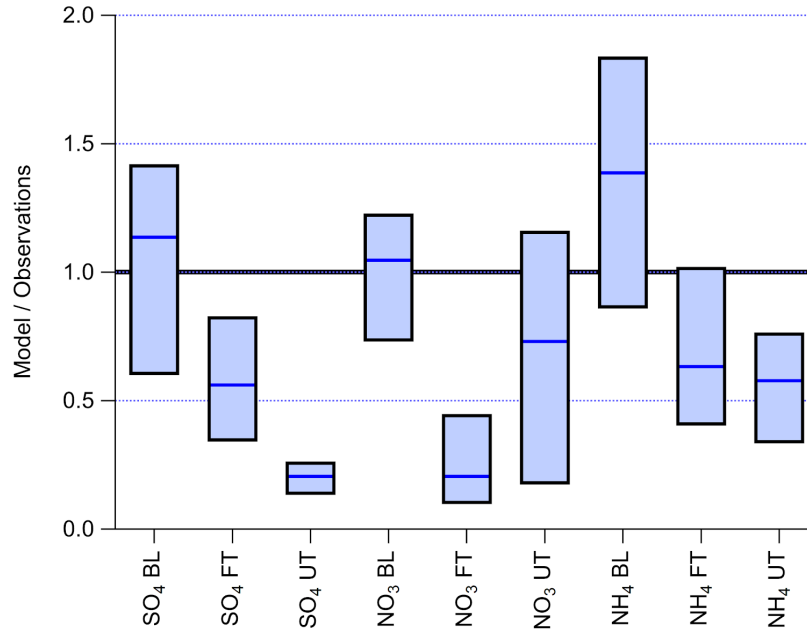
404 Supplemental Figures

405

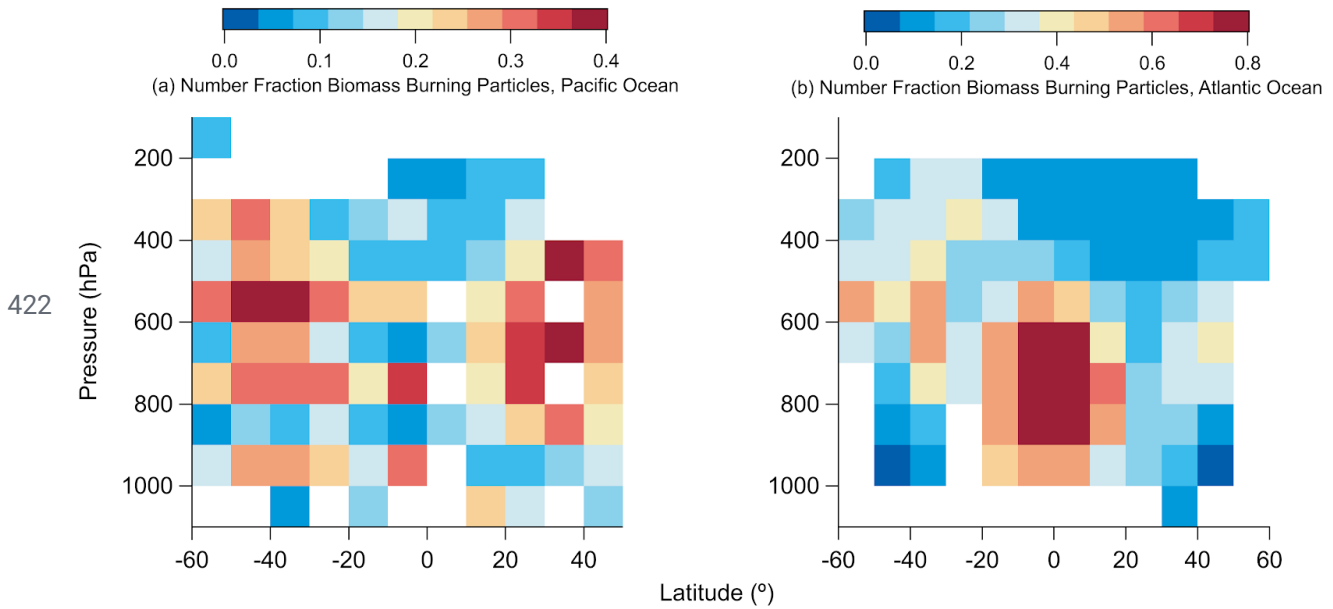


407 Supplemental Figure 1. Map of flight campaigns along with average aerosol molar
 408 composition for each campaign. Flight tracks and average inorganic aerosol composition, in
 409 molar charge equivalents ($\text{NH}_4/18$ (orange), $\text{NO}_3/62$ (blue), and $2 \times \text{SO}_4/96$ (red)), for each
 410 campaign and different oceanic locations for ATom-1 and -2 (Supplemental Table 2). The
 411 average inorganic mass concentrations are listed above each pie chart, where sm^{-3} is standard
 412 meters cubed at constant temperature (273.15 K) and pressure (1013 hPa) (STP).

413

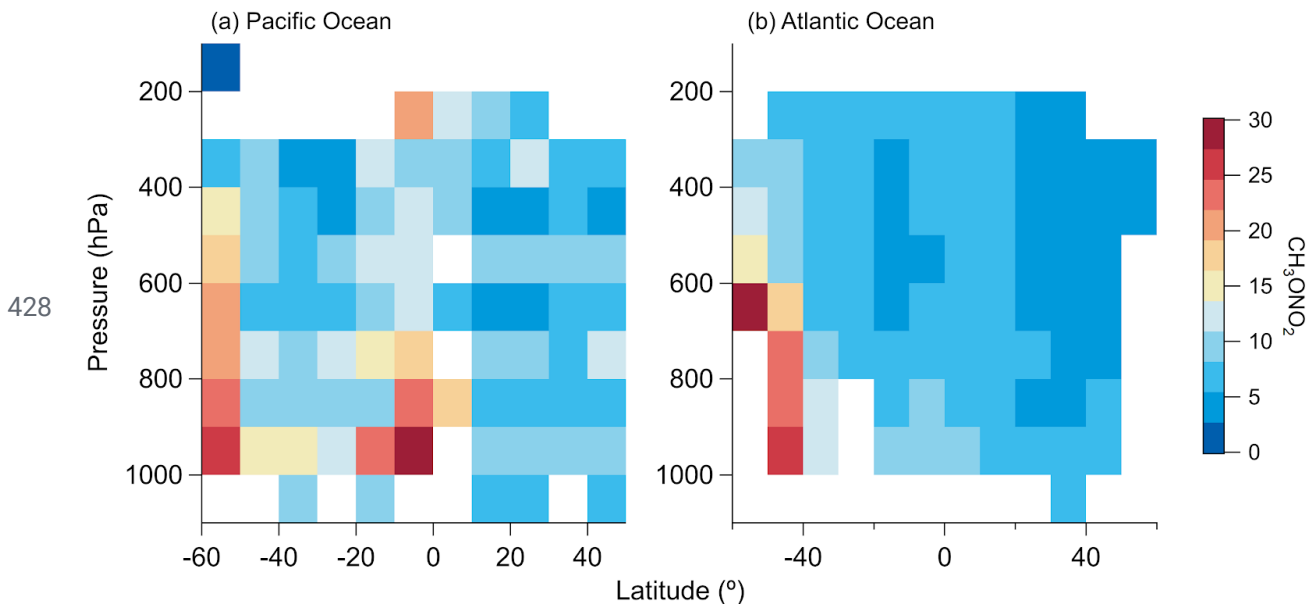


414 *Supplemental Figure 2. Comparison of model to observed aerosol concentration by species and*
 415 *altitude. Same as Fig. 2. Box plot for the ratios between AeroCom-II modeled and observed*
 416 *sulfate (SO₄), nitrate (NO₃), and ammonium (NH₄) for boundary layer (BL, surface to 800 hPa),*
 417 *free troposphere (FT, 800 to 400 hPa), and upper troposphere (UT, 400 to 250 hPa) for all*
 418 *campaigns not in urban regions (i.e., not CalNex, KORUS-AQ, MILAGRO, and WINTER)*
 419 *evaluated here and for AeroCom-II CTMs (CCSM4, GISS-MATRIX, GISS-ModelE, and*
 420 *TM4-ECPL-F). The blue horizontal line is the median ratio of the model-to-observations*
 421 *ensemble, and the boxes are the 25th and 75th percentiles. For data used here, see the SI File.*

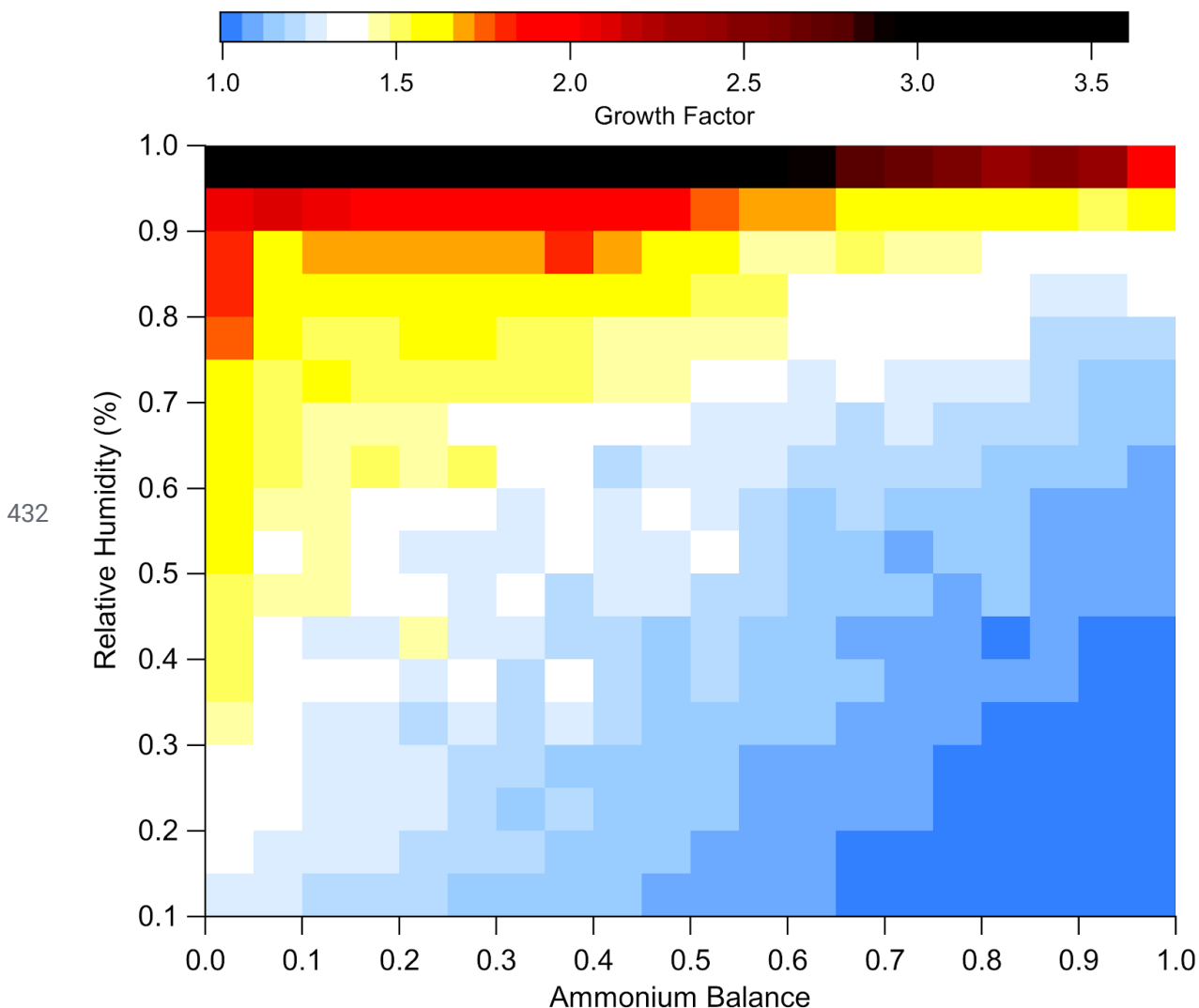


423 *Supplemental Figure 3. Curtain plot of biomass burning marker for Pacific and Atlantic*
 424 *Ocean. Curtain plot of number fraction of aerosol measured as biomass burning, from the NOAA*
 425 *single particle mass spectrometer (PALMS)³⁰, for ATom-1 and -2, over the Pacific (a) and*
 426 *Atlantic (b) oceans.*

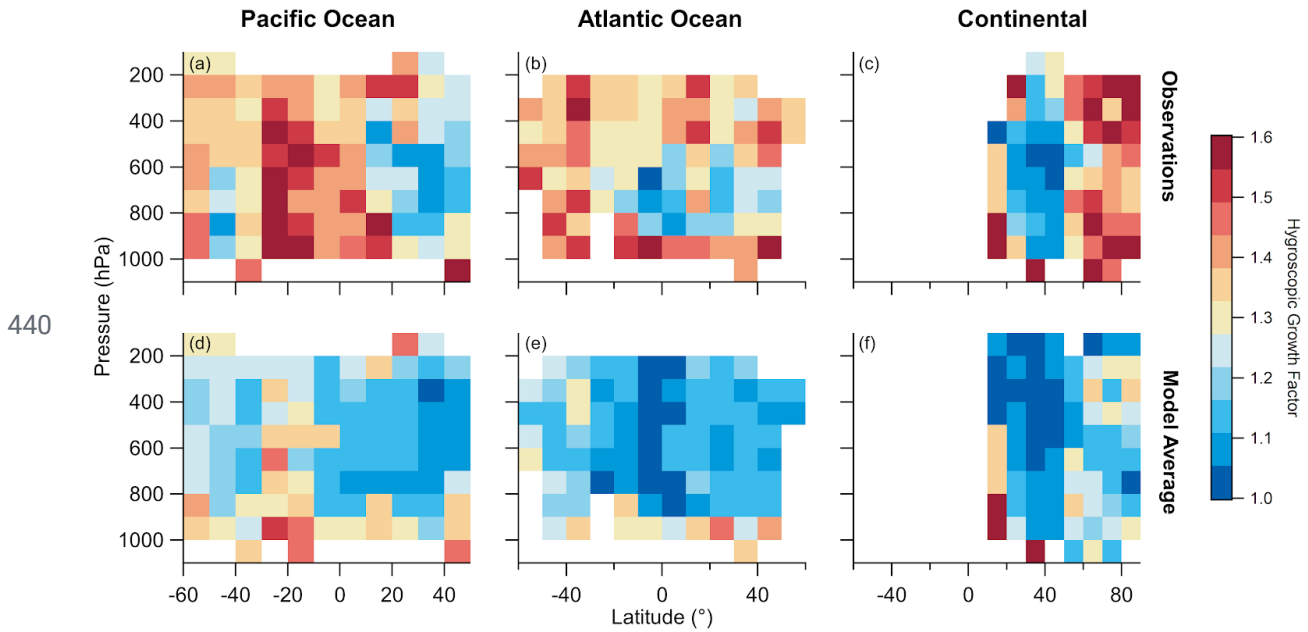
427



429 *Supplemental Figure 4. Curtain plot of methyl nitrate for Pacific and Atlantic Ocean. Curtain*
 430 *plot of methyl nitrate (CH_3ONO_2) measured by University of California, Irvine, whole air*
 431 *sampler¹⁰⁶ for ATom-1 and -2, over the Pacific (a) and Atlantic (b) oceans.*

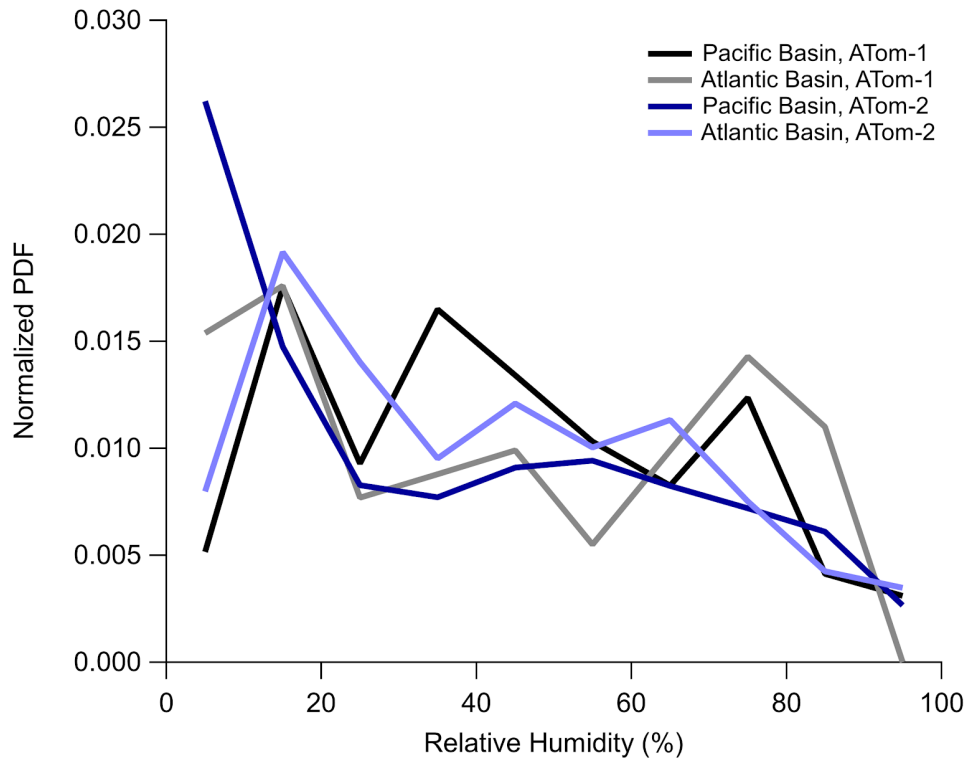


433 *Supplemental Figure 5. Behavior of observationally constrained HGF as a function of relative*
 434 *humidity and ammonium balance. Predicted hygroscopic growth factor (HGF) for measured*
 435 *ammonium, nitrate, and sulfate, averaged across campaigns analyzed here (Supplemental Table*
 436 *2), as a function of relative humidity (left) and ammonium balance ($n\text{NH}_4 / (2 \times n\text{SO}_4 + n\text{NO}_3)$).*
 437 *See Section S2 on details pertaining to the calculation of growth factor. Briefly, HGF was*
 438 *calculated for all data observed (1-minute data) and then binned the calculated HGF as a*
 439 *function of RH and NH_4_{Bal} .*



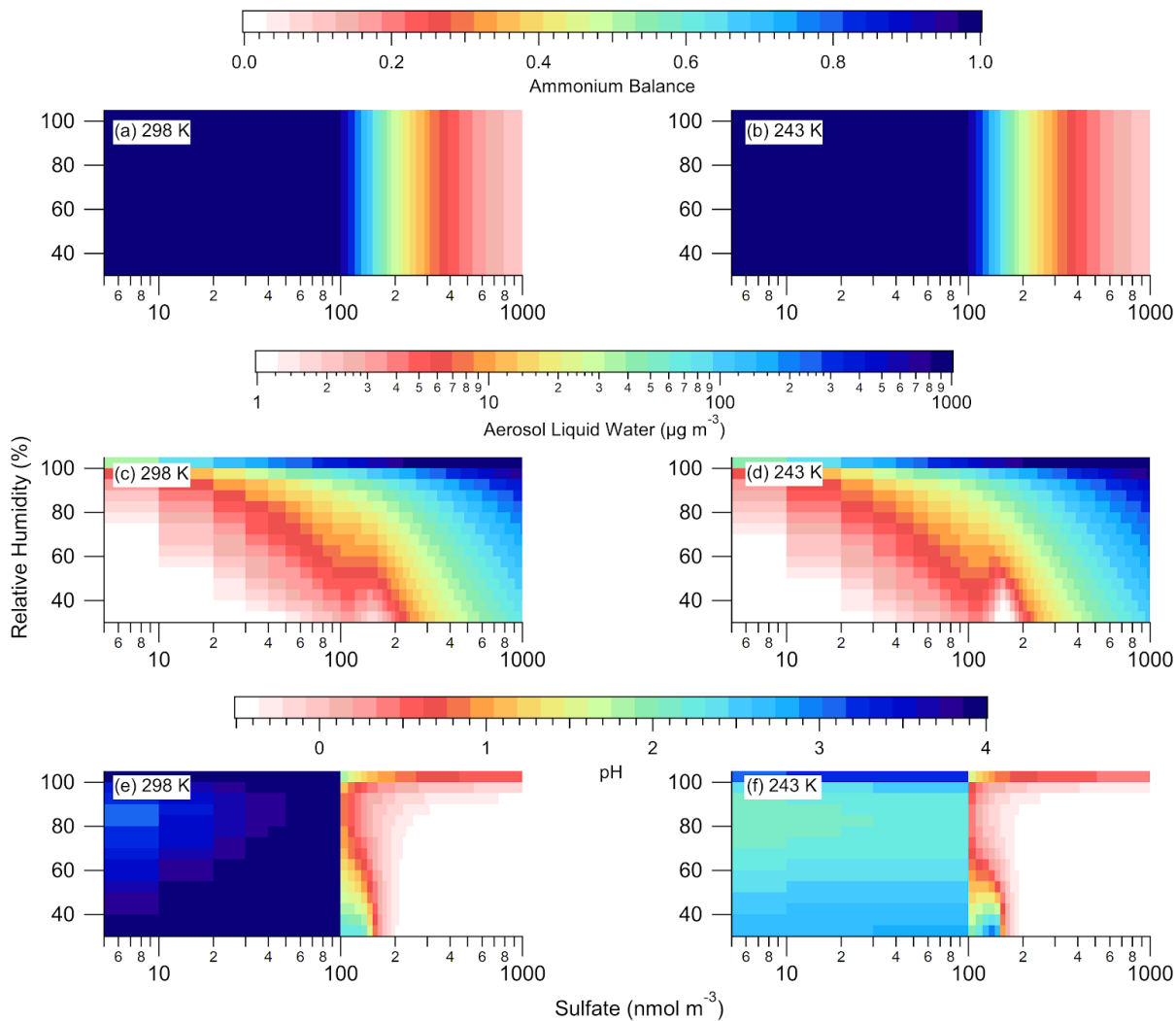
441 *Supplemental Figure 6. Curtain plot of observationally constrained and modeled predicted*
 442 *HGF. Curtain plot of the calculated hygroscopic growth factor for the average (a-c)*
 443 *observations and (d-f) CTMs over the Pacific and Atlantic basins (ATom-1 and -2) and other*
 444 *campaigns (Continental). See Section S2 on details pertaining to the calculation of the growth*
 445 *factor. The HGF shown in Supplemental Figure 6 for the CTMs was calculated by using the*
 446 *average RH and NH_{4_Bal} to estimate the HGF from the look-up table (Supplemental Figure 5).*

447

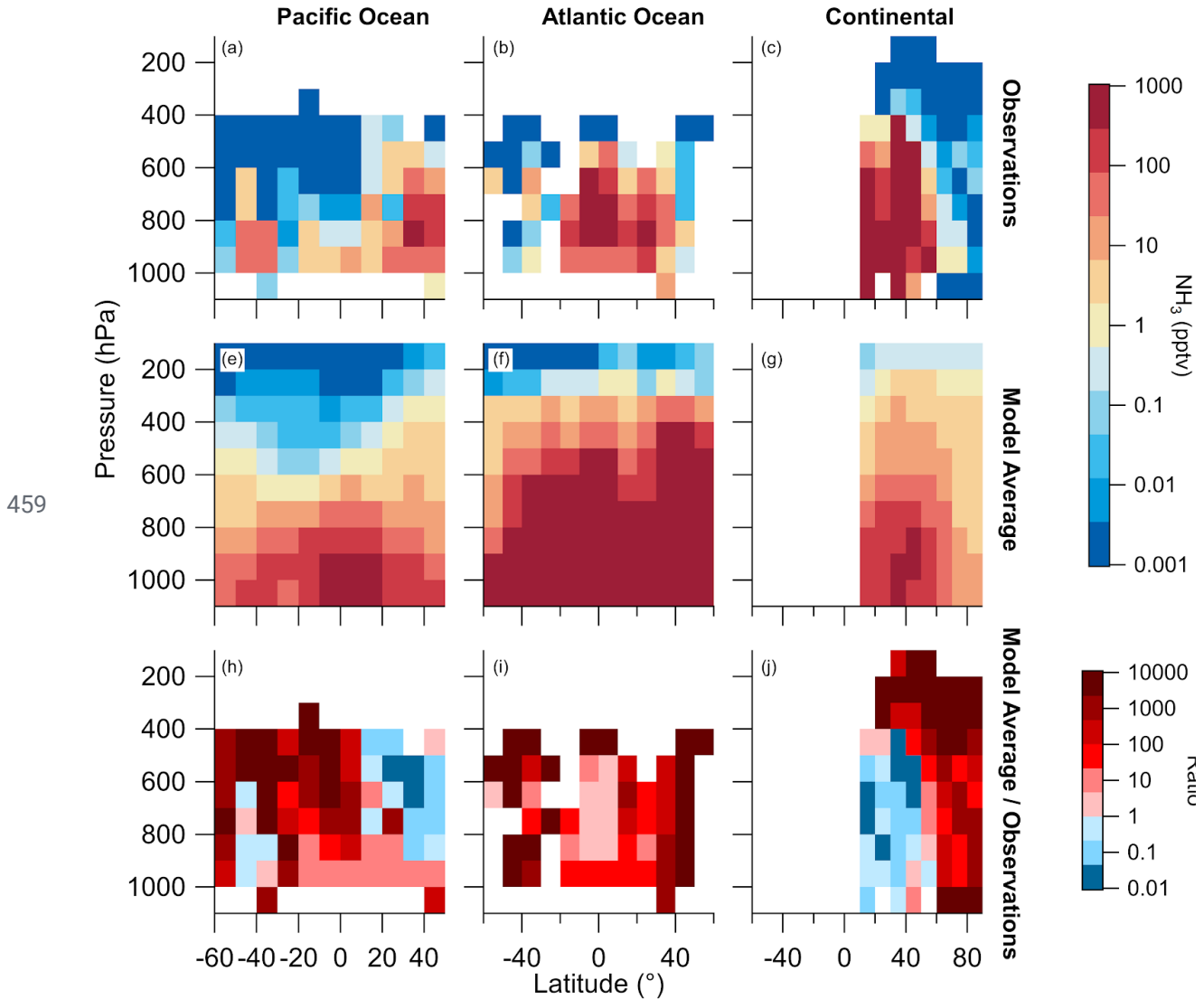


448 *Supplemental Figure S7. Probability distribution function of relative humidity for remote*
449 *oceanic basins. Normalized probability distribution function (PDF) of the relative humidities for*
450 *the Pacific and Atlantic Basins during ATom-1 and -2. Black is Pacific Basin for ATom-1, grey is*
451 *Atlantic Basin for ATom-1, dark blue is Pacific Basin for ATom-2, and light blue is Atlantic Basin*
452 *for ATom-2.*

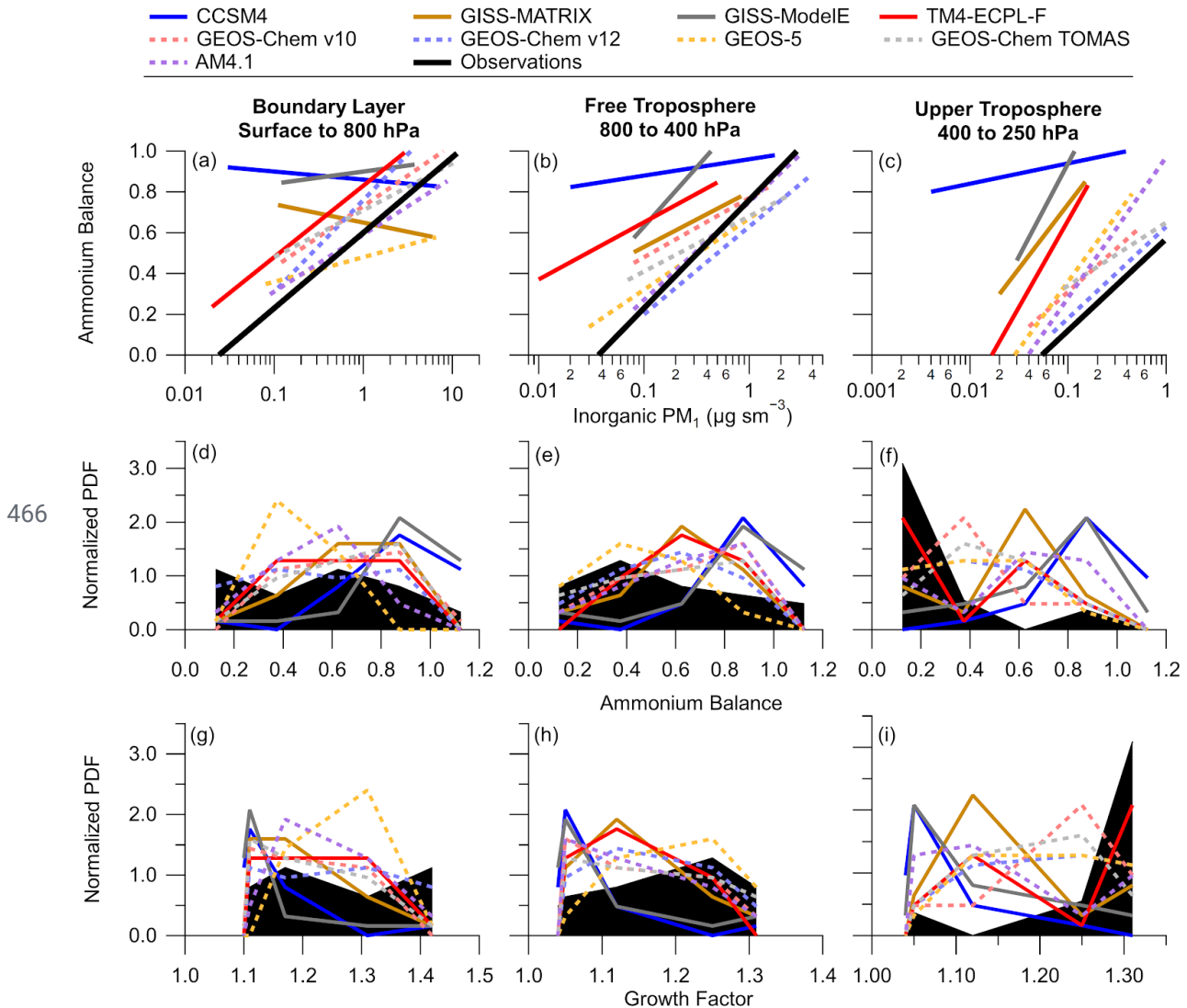
453



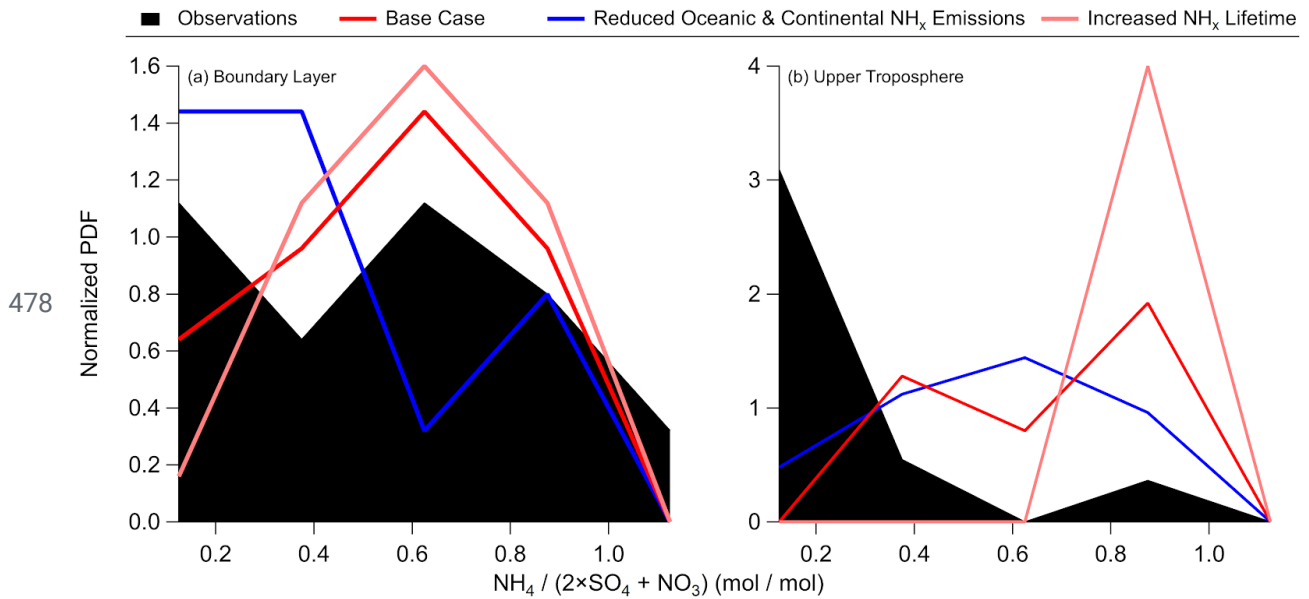
454 *Supplemental Figure 8. Predicted behavior of aerosol properties using a box model. Results*
 455 *from a box model calculation for aerosol pH using E-AIM, where total ammonium ($NH_{3,g} +$*
 456 *$NH_{4,p}$) remained constant at 200 nmol m^{-3} , sulfate varied between 5 to 1000 nmol m^{-3} , relative*
 457 *humidity varied between 30 to 95%, and temperature varied between 298 K ((a), (c), and (e))*
 458 *and 243 K ((b), (d), and (f)).*



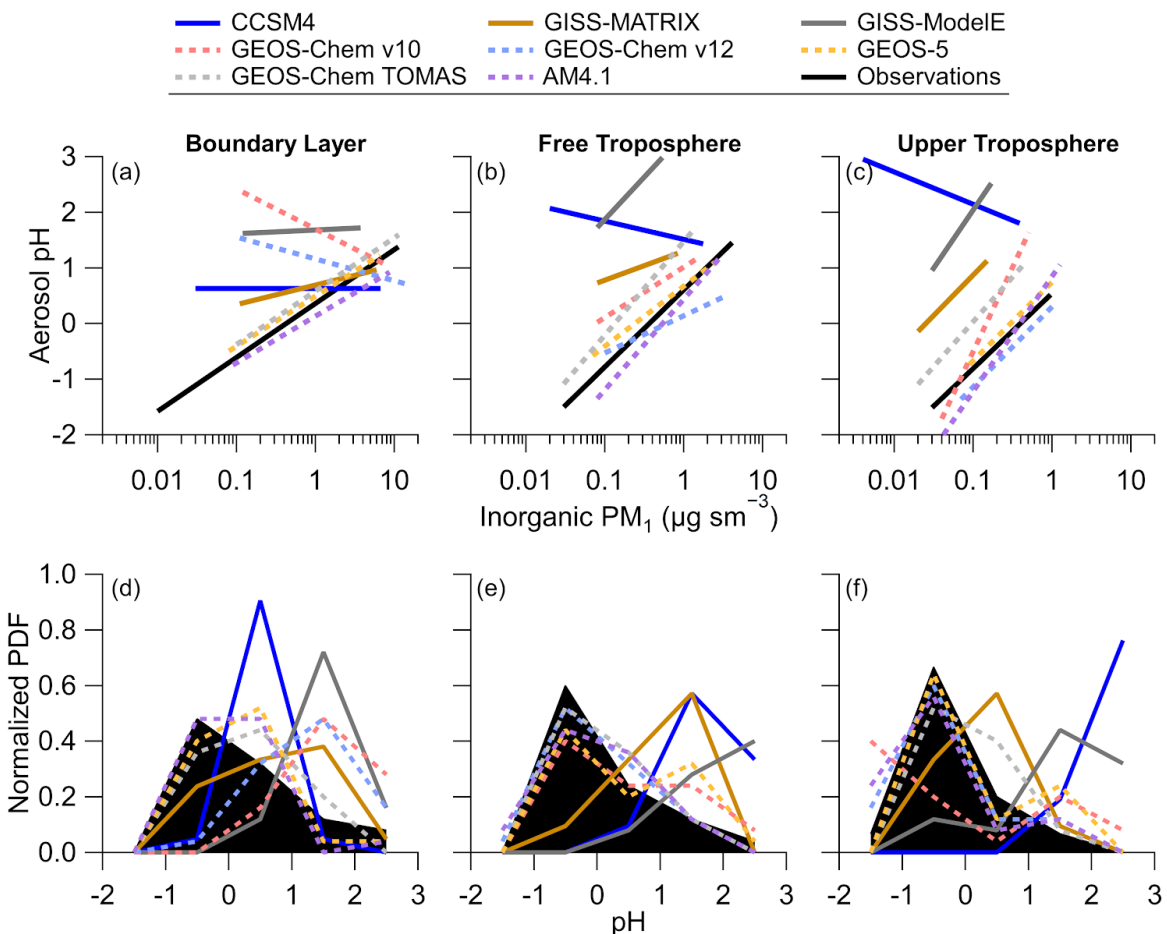
460 *Supplemental Figure 9. Curtain plot of observationally constrained and CTM predicted*
 461 *ammonia. Curtain plot of observationally constrained ammonia from E-AIM (a-c), average*
 462 *CTMs ammonia (d-f), and ratio of CTMs-to-observations for Pacific Ocean (g), Atlantic Ocean*
 463 *(h) and Continental regions (i), as defined in Supplemental Table 2. The models that had*
 464 *ammonia as output were used in the curtain plots and include GEOS-Chem v10, GEOS-Chem*
 465 *v12, GEOS-Chem TOMAS, GEOS-5, and AM4.1 (Supplemental Table 4).*



467 **Supplemental Figure 10. Comparison of slopes and probability distribution functions for all**
 468 **models and observations.** Full results for Fig. 5. (a–c) Comparison of NH_{4_Bal} versus
 469 $\log_{10}(\text{inorganic } PM_{10})$ slopes from observations (black) and models (Supplemental Table 5 and
 470 Supplemental Table 6). (d–f) Normalized probability distribution function (PDF) of NH_{4_Bal} for
 471 observations (solid black) and models. (g–i) Normalized PDF of estimated HGF for observations
 472 (solid black) and models, using the values from Supplemental Figure 5, and average values RH
 473 from observations ($\sim 50\%$, $\sim 35\%$, and $\sim 35\%$ for BL, FT, and UT, respectively). For all figures, the
 474 AeroCom-II models are solid and the post-AeroCom-II models are dashed. Blue solid is CCSM4,
 475 gold solid is GISS-MATRIX, grey solid is GISS-ModelE, red solid is TM4-ECPL-F, light red
 476 dashed is GEOS-Chem v10, light blue dashed is GEOS-Chem v12, orange dashed is GEOS-5,
 477 grey dashed is GEOS-Chem TOMAS, purple dashed is AM4.1, and black solid is observations.

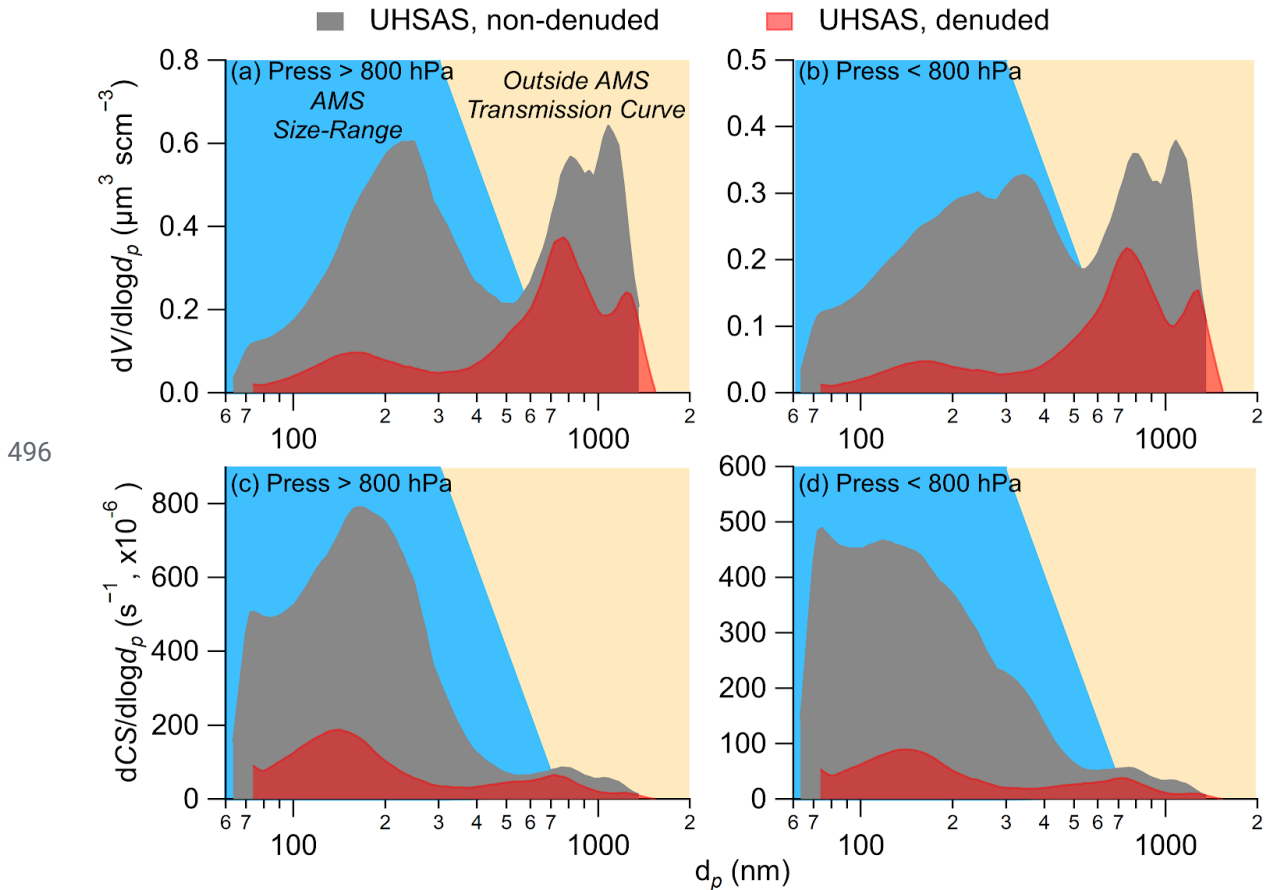


479 *Supplemental Figure 11. Probability distribution function results from observations and*
 480 *various GEOS-Chem cases studies, where various factors impacting ammonium were*
 481 *explored. Similar to Supplemental Figure 10d-f, but normalized probability distribution function*
 482 *of ammonium balance from GEOS-Chem v12 total ammonia sensitivity cases (Supplemental*
 483 *Table 7) for (a) Boundary Layer (surface to 800 hPa) and (b) Upper Troposphere (400 to 250*
 484 *hPa). Black is observations, red is base case, blue is reduced oceanic and continental NH_x*
 485 *emissions, and light red is increased NH_x lifetime.*



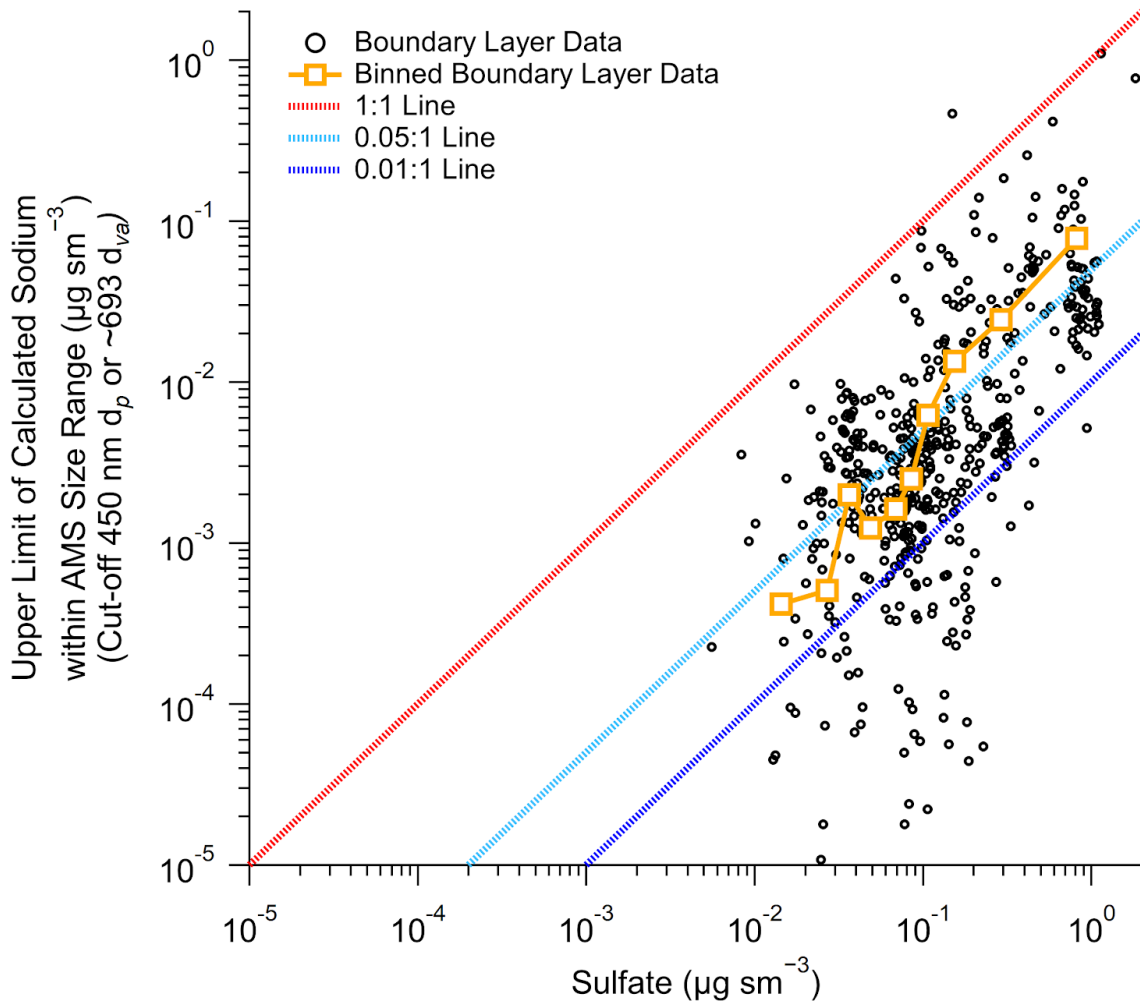
486

487 *Supplemental Figure 12. Comparison of slopes and probability distribution functions for all*
 488 *models and observations. Full results for Fig. 6. (a–c) Comparison of pH versus*
 489 *log₁₀(inorganic PM₁) slopes from observations (black) and models (Supplemental Table 5 and*
 490 *Supplemental Table 6). (d–f) Normalized PDF of pH for observations (solid black) and models.*
 491 *BL = surface-800 hPa, FT = 800-400 hPa, and UT = 400-250 hPa. For all figures, the*
 492 *AeroCom-II models are solid and the post-AeroCom-II models are dashed. Blue solid is CCSM4,*
 493 *gold solid is GISS-MATRIX, grey solid is GISS-ModelE, light red dashed is GEOS-Chem v10,*
 494 *light blue dashed is GEOS-Chem v12, orange dashed is GEOS-5, grey dashed is GEOS-Chem*
 495 *TOMAS, purple dashed is AM4.1, and black solid is observations.*



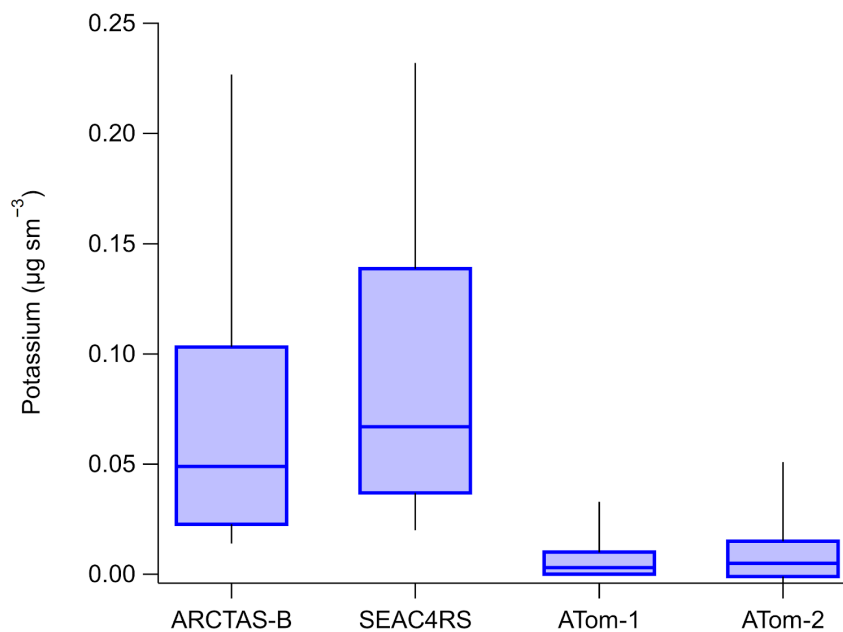
497 **Supplemental Figure 13 Investigation into the influence of non-volatile cations in the volume**
 498 **distribution and condensational sink during ATom.** Average volume distribution (a,b) and
 499 condensational sink distribution (c,d) of measured total aerosol (UHSAS, non-denuded, grey)
 500 and nonvolatile/refractory aerosol (UHSAS, denuded, red) during ATom-2 for air sampled within
 501 marine boundary layer (pressure > 800 hPa, (a) & (c)) and in free/upper troposphere (pressure
 502 < 800 hPa, (b) & (d)). The transmission curve (defining diameters of aerosol observed by AMS),
 503 from Guo et al.²⁰, is shown in blue, and the aerosol not observed by AMS is shown in tan.

504

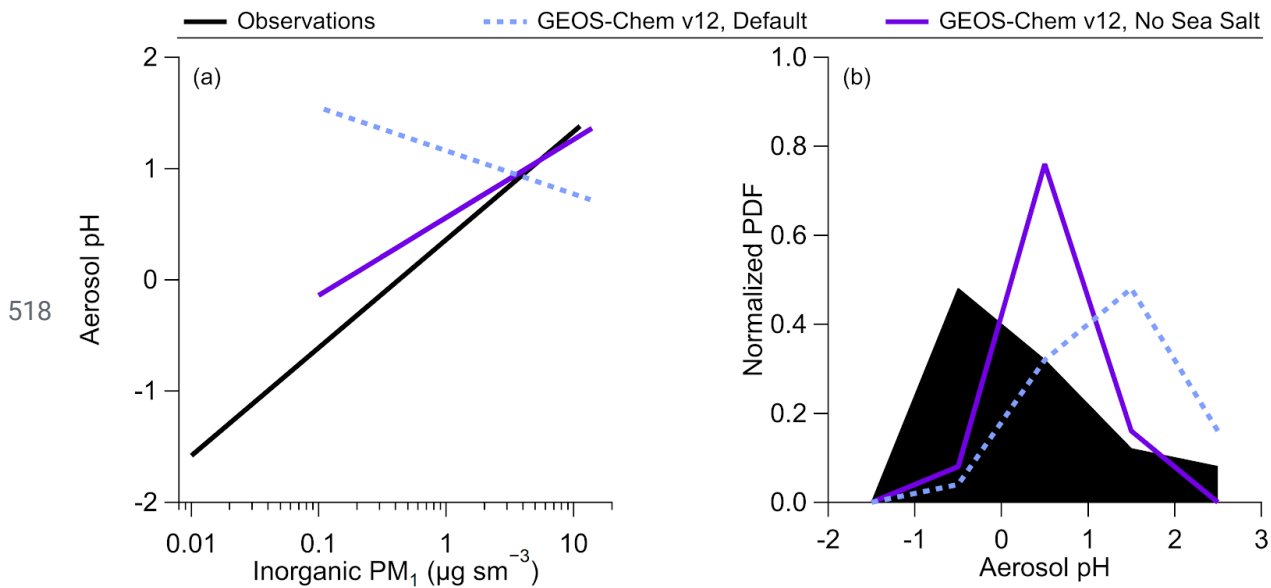


505 *Supplemental Figure 14. Comparison of predicted submicron sodium with sulfate measured by*
 506 *the AMS during ATom.* Scatter plot of calculated sodium mass concentration (see Sect. S4.4 for
 507 *details on calculation), for geometric diameters up to 450 nm (the 50% diameter cut-off for*
 508 *AMS²⁰) versus measured sulfate, in the boundary layer (surface to 800 hPa) during ATom-2.*
 509 *Black circles are all data in the boundary layer, orange square is the binned data, red dashed is*
 510 *the 1:1 line, light blue is 0.05:1 line, and blue dashed is 0.01:1 line.*

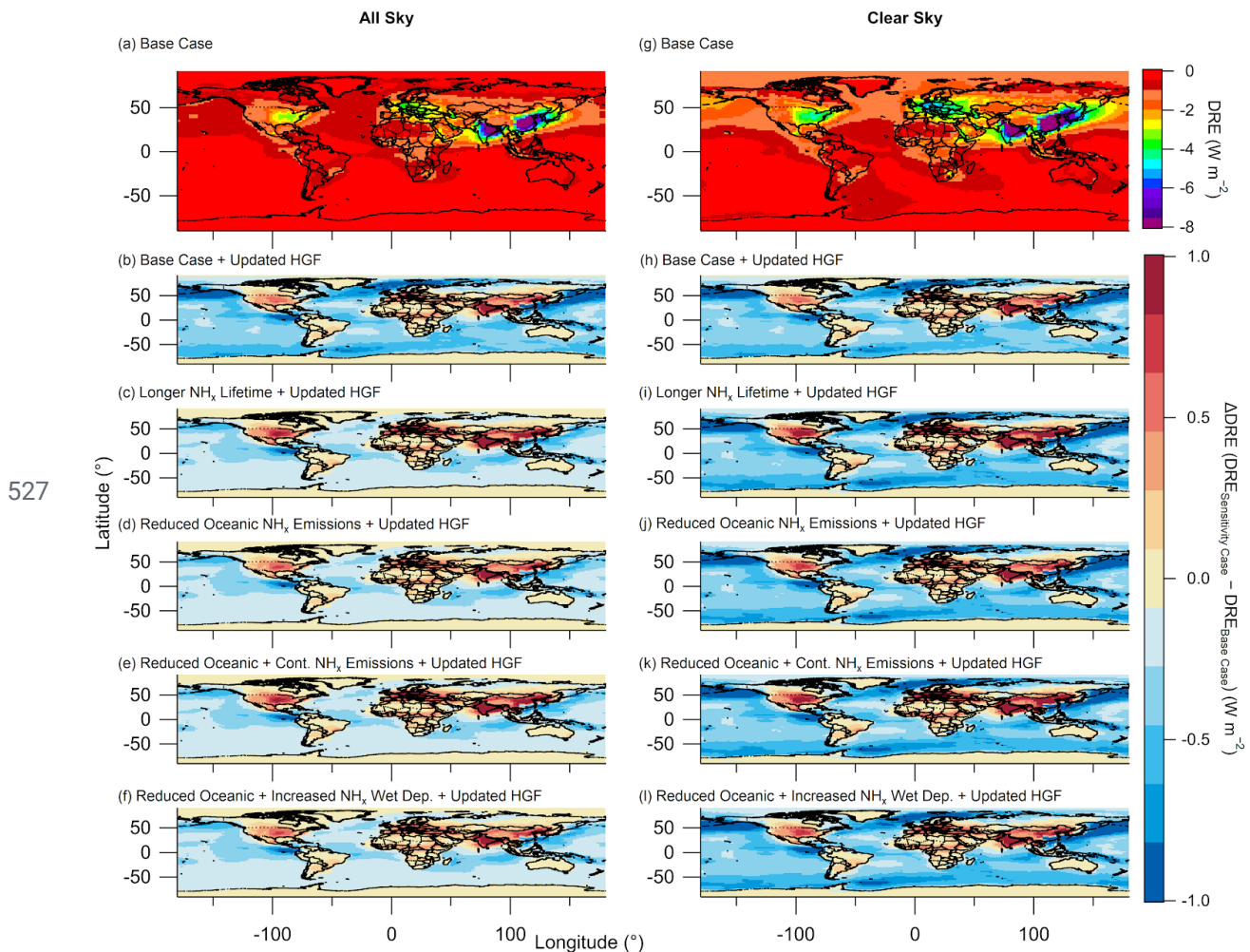
511



512 *Supplemental Figure 15. Comparison of potassium mass concentrations from various*
513 *campaigns. Box-and-whisker plot for the potassium mass concentration measured during two*
514 *campaigns focused on biomass burning (ARCTAS-B and SEAC⁴RS) and two campaigns focused*
515 *on remote atmosphere (ATom-1 and -2). Potassium was collected onto Teflon filters and analyzed*
516 *off-line by ion chromatography^{107,108}.*

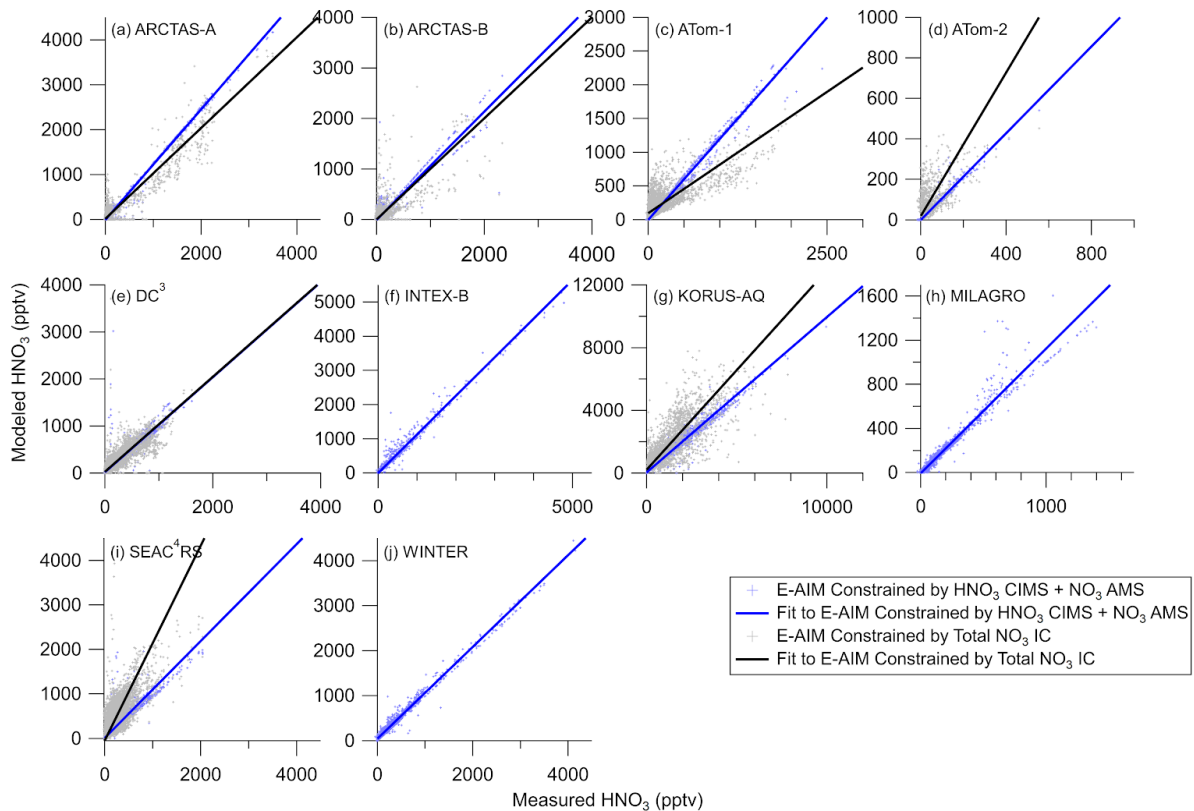


519 *Supplemental Figure 16. Investigation in the impacts of removing sea-salt in the calculation of*
 520 *aerosol pH for GEOS-Chem. (a) Comparison of aerosol pH versus \log_{10} (inorganic PM₁ (sulfate*
 521 *+ nitrate + ammonium)) slopes from observations (black) and default GEOS-Chem (light blue*
 522 *dashed), and GEOS-Chem with sea-salt excluded from the pH calculation (purple) for the*
 523 *boundary layer (surface to 800 hPa). (b) Normalized probability distribution function of aerosol*
 524 *pH for observations (solid black) and default GEOS-Chem and GEOS-Chem with sea-salt*
 525 *excluded for the boundary layer.*



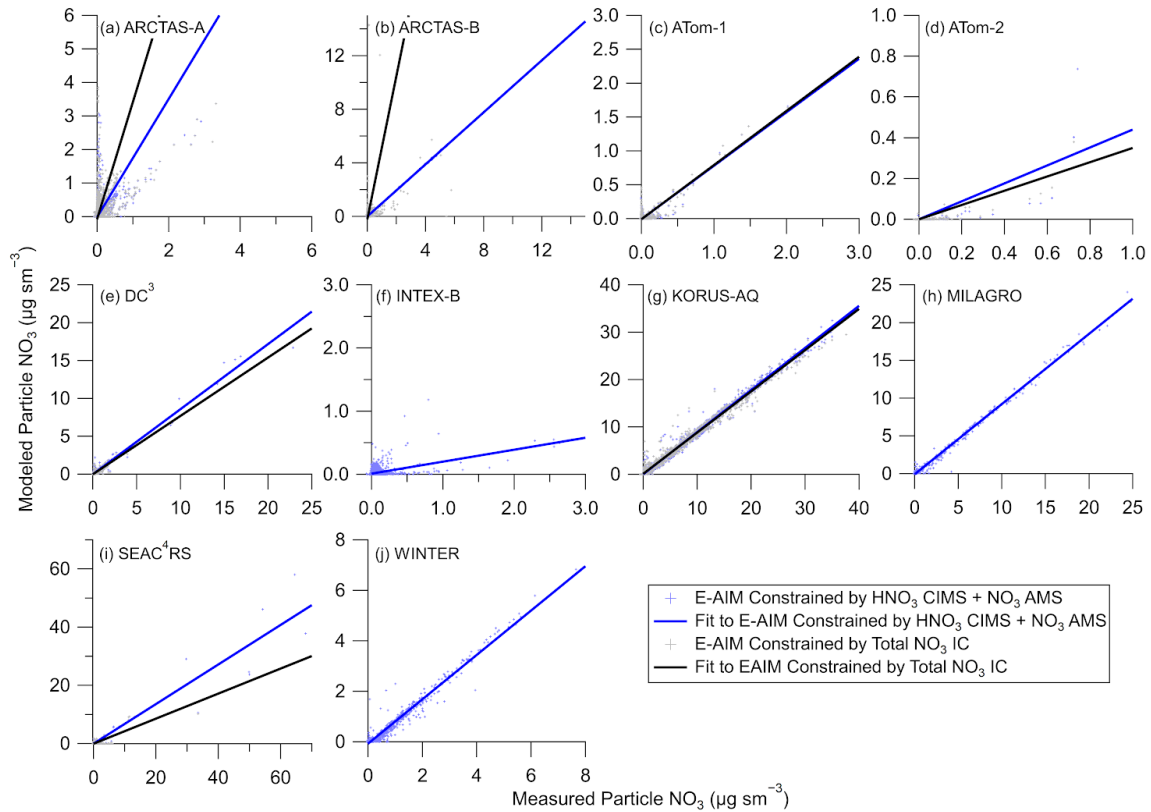
528 *Supplemental Figure 17. Changes in the direct radiative effect from the base case with*
 529 *different cases in calculating HGF and ammonium mass concentration. Calculated, annually*
 530 *averaged, short wave direct radiative forcing (DRE) from sulfate, nitrate, and ammonium (and*
 531 *associated water), from GEOS-Chem, for all sky (left column) and clear sky (right column) (a,g)*
 532 *Base Case, (b,h) Base Case with updated HGF, (c,i) decreased Henry's law constant (H) for*
 533 *increased wet deposition lifetime with updated HGF, (d,j) reduced NH_x oceanic emissions with*
 534 *updated HGF, (e,k) reduced NH_x oceanic and continental emissions with updated HGF, and (f,l)*
 535 *reduced NH_x oceanic emissions, increased Henry's law constant (H) for decreased wet deposition*
 536 *lifetime, and updated HGF. See Supplemental Table 7 for description of the different cases and*
 537 *Fig. 7 for annual average DRE.*

538



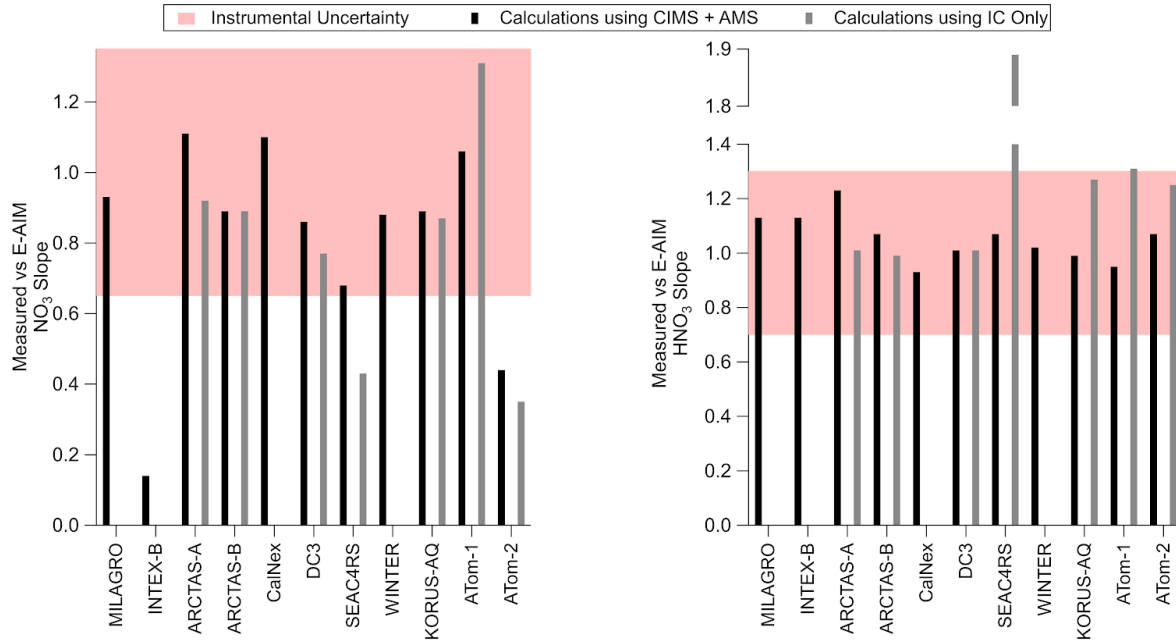
539 **Supplemental Figure 18. Comparison of E-AIM predicted and observed nitric acid from all**
 540 **campaigns.** Scatter plot of modeled (E-AIM) versus measured gas-phase HNO_3 for the
 541 campaigns used here (Supplemental Table 2). For campaigns with more than one gas-phase
 542 HNO_3 measurements (Supplemental Table 3), the comparison of modeled and gas-phase HNO_3
 543 from the input of both is shown in the scatter plot, where light blue is from CIMS HNO_3 and AMS
 544 NO_3 and grey is from IC NO_3 . For values of the slopes, see Supplemental Figure 20. Regressions
 545 shown are ODR, where blue is for CIMS + AMS and black is for IC.

546



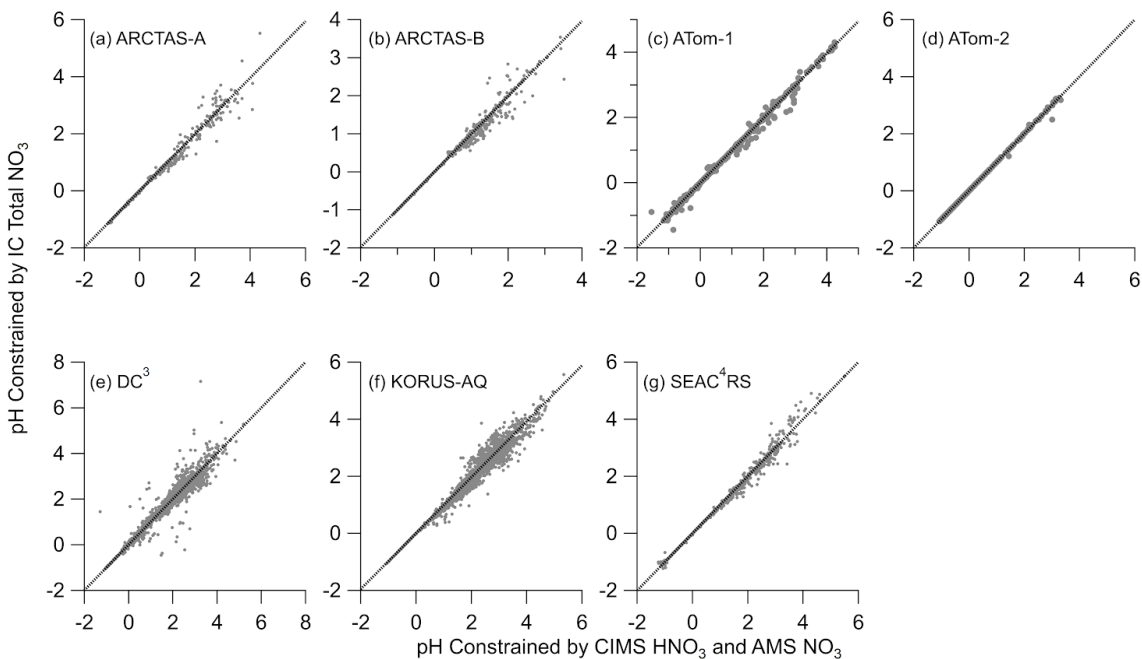
547 *Supplemental Figure 19. Comparison of E-AIM predicted and observed nitrate from all*
 548 *campaigns. Same as Supplemental Figure 18, but for particle-phase NO_3^- . For values of the*
 549 *slopes, see Supplemental Figure 20. Regressions shown are ODR.*

550



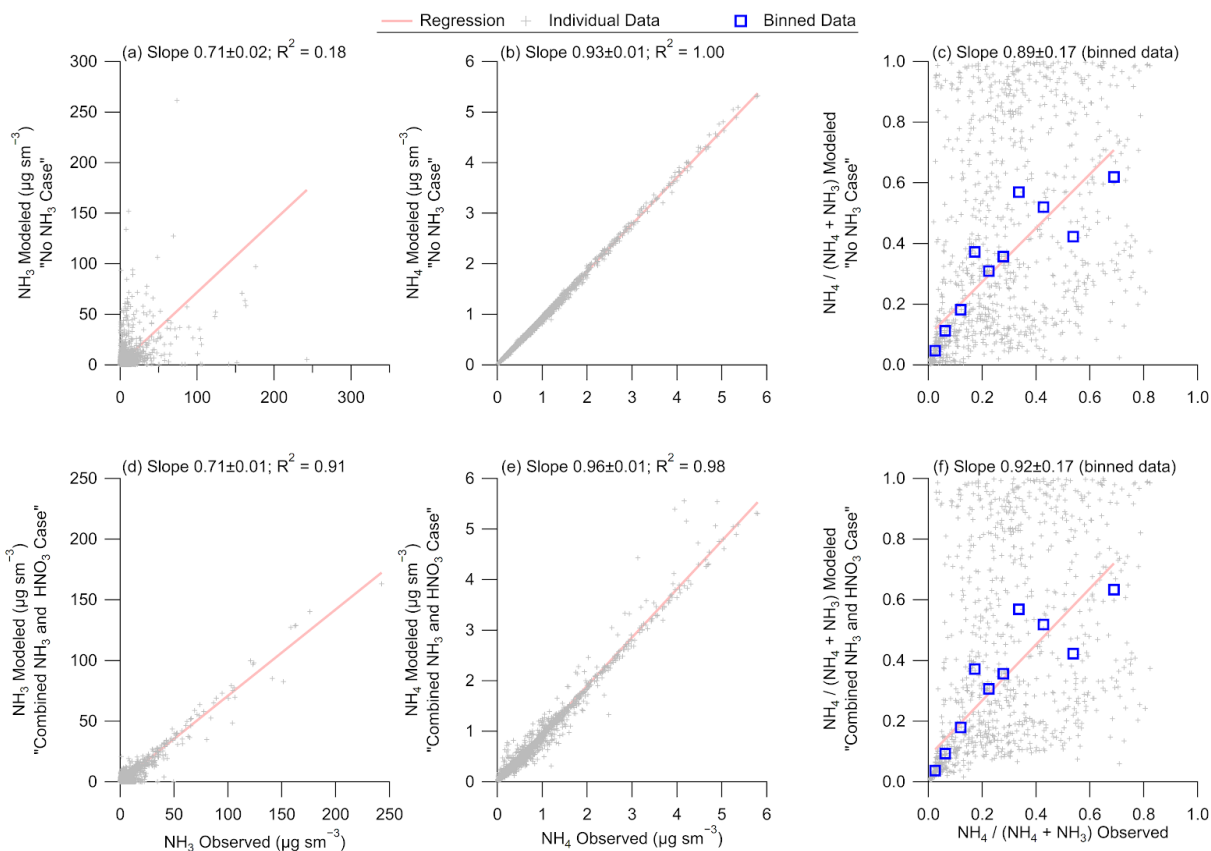
551 *Supplemental Figure 20. Comparison of E-AIM predicted and observed nitric acid and nitrate*
 552 *from all campaigns. Comparison of slopes from Supplemental Figure 18 and 19 for the different*
 553 *campaigns along with the uncertainties from the measurements (red shaded) of particle-phase*
 554 *NO₃⁻ and gas-phase HNO₃. Black lines are for results using CIMS + AMS and grey is using*
 555 *results from IC only.*

556



557

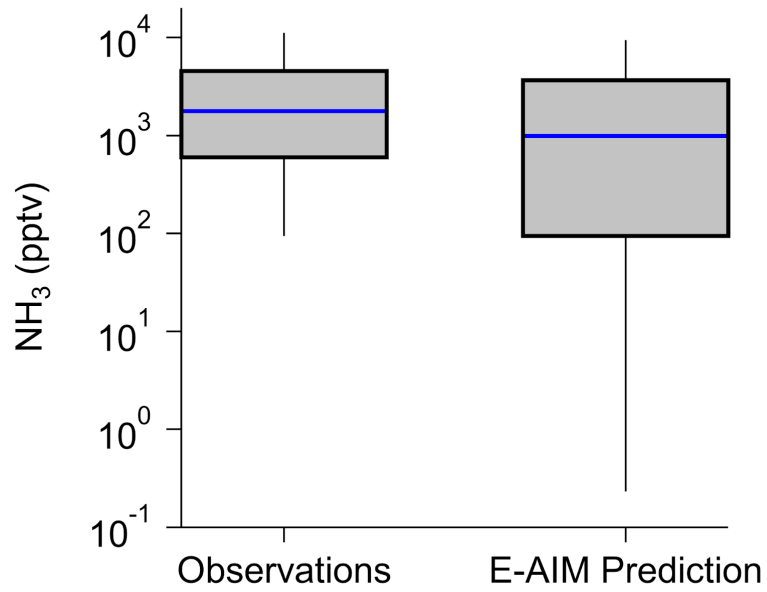
558 *Supplemental Figure 21. Comparison of E-AIM predicted pH using different total nitrate*
 559 *inputs. Scatter plot of pH constrained by total nitrate from MC/IC and from CIMS HNO₃ plus*
 560 *AMS NO₃. This is only for campaigns where both total nitrate measurements were available*
 561 *(Supplemental Table 3). Regressions shown are ODR.*



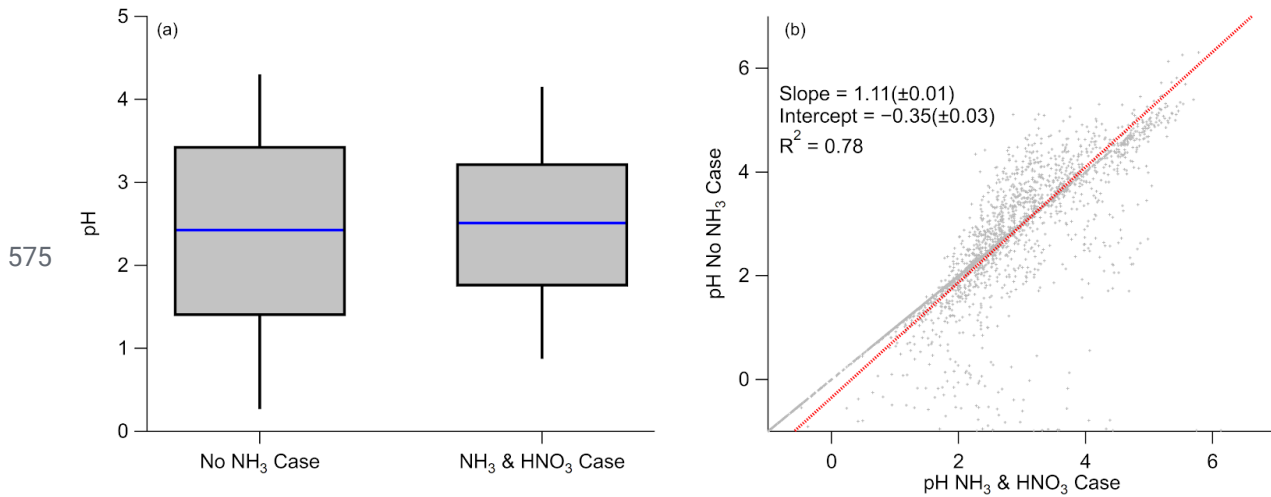
562

563 *Supplemental Figure 22. Evaluation in the performance of E-AIM with and without ammonia*
 564 *as input into the calculations. Evaluation of predicted versus observed ammonia (a and d),*
 565 *ammonium (b and e), and fraction of ammonium to total (ammonia plus ammonium) (c and f) for*
 566 *E-AIM model constrained without measured ammonia (top) and with measured ammonia*
 567 *(bottom). The evaluation is for the CalNex campaign (Supplemental Table 3), the only campaign*
 568 *used here that had measurements of ammonia. Regression shown is the least-orthogonal-distance*
 569 *regression fitting method (ODR) of the data. Blue squares in (c,f) are binned decile data.*

570

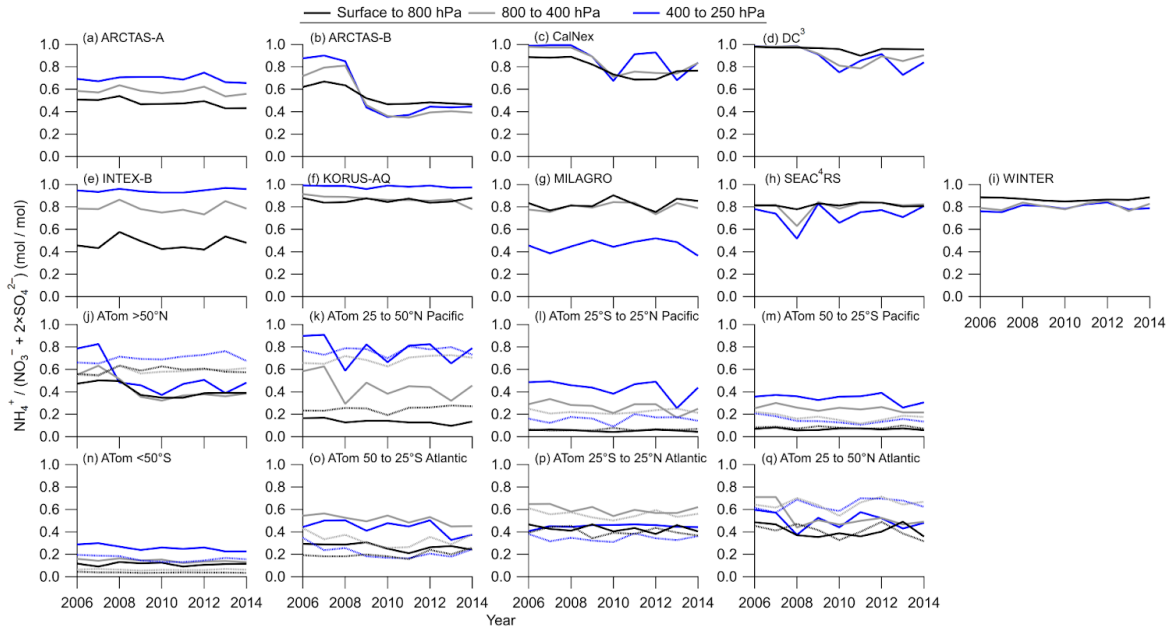


571 *Supplemental Figure 23. Comparison of the observed and predicted ammonia during CalNex.*
572 *Box and whisker plot of observed and E-AIM model ammonia predicted mixing ratios for*
573 *CalNex. Blue line is the median (50th percentile), box is 25th and 75th percentile, and whisker is*
574 *the 10th and 90th percentile.*



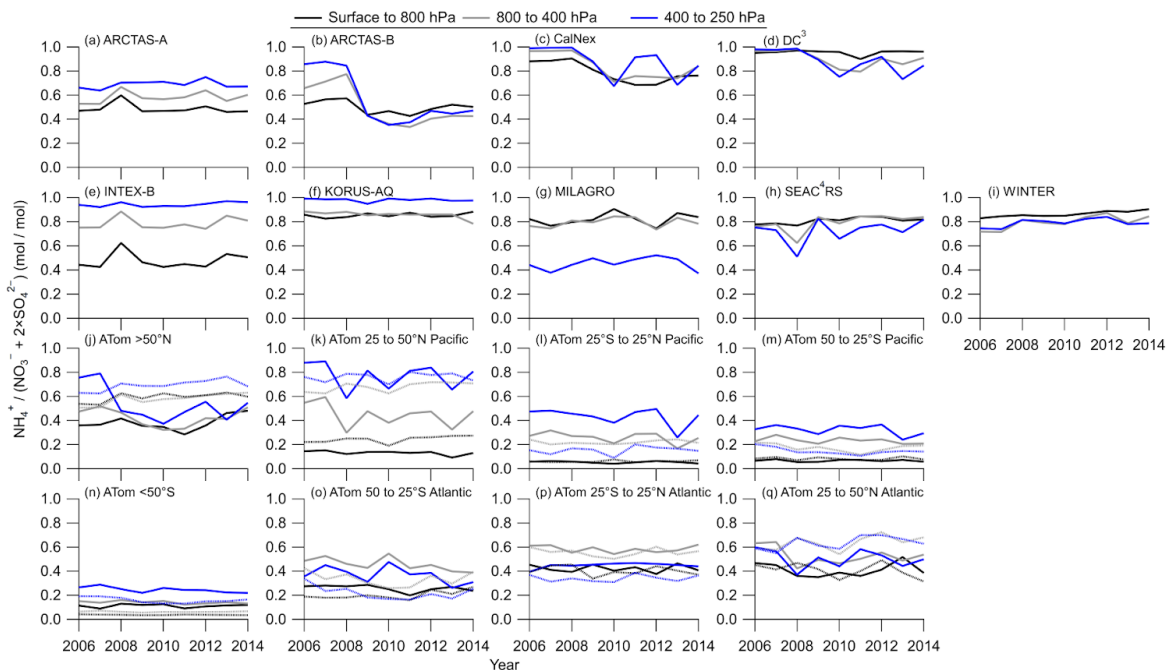
576 *Supplemental Figure 24. Comparison in the performance of E-AIM in predicting pH with and*
 577 *without ammonia as input. (a) Box and whisker plot of predicted pH from CalNex with input not*
 578 *including and including gas-phase ammonia. The blue line is the median (50th percentile), box*
 579 *uses the 25th and 75th percentiles, and the whiskers are the 10th and 90th percentile. (b) Scatter*
 580 *plot of the two cases, where the regression is ODR. Red line is the fit.*

581



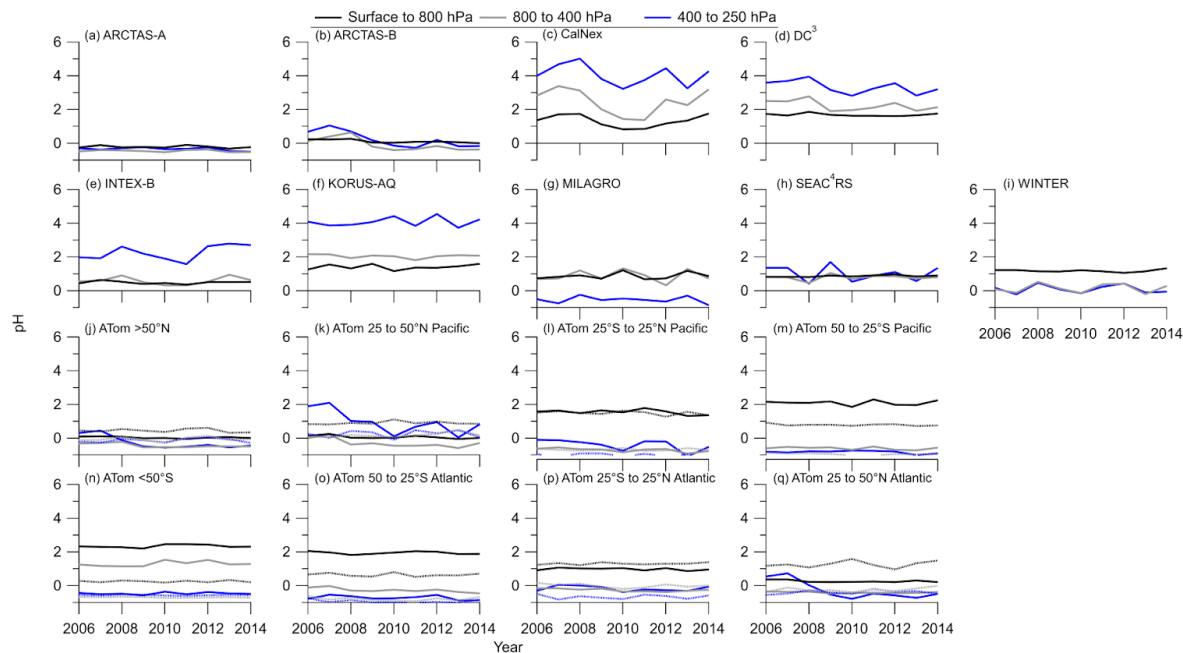
582 *Supplemental Figure 25. Evaluation in the predicted trends of ammonium balance over a*
 583 *decade with emissions constant. NH_4 from GEOS-Chem, from 2006 to 2014, with emissions*
 584 *for 2010, for the three pressure levels in the troposphere (surface to 800 (black), 800 to 400*
 585 *(grey), and 400 to 250 (blue) hPa), for the regions defined in Supplemental Table 2. For the*
 586 *ATom regions, solid is for ATom-1 and dashed is for ATom-2.*

587



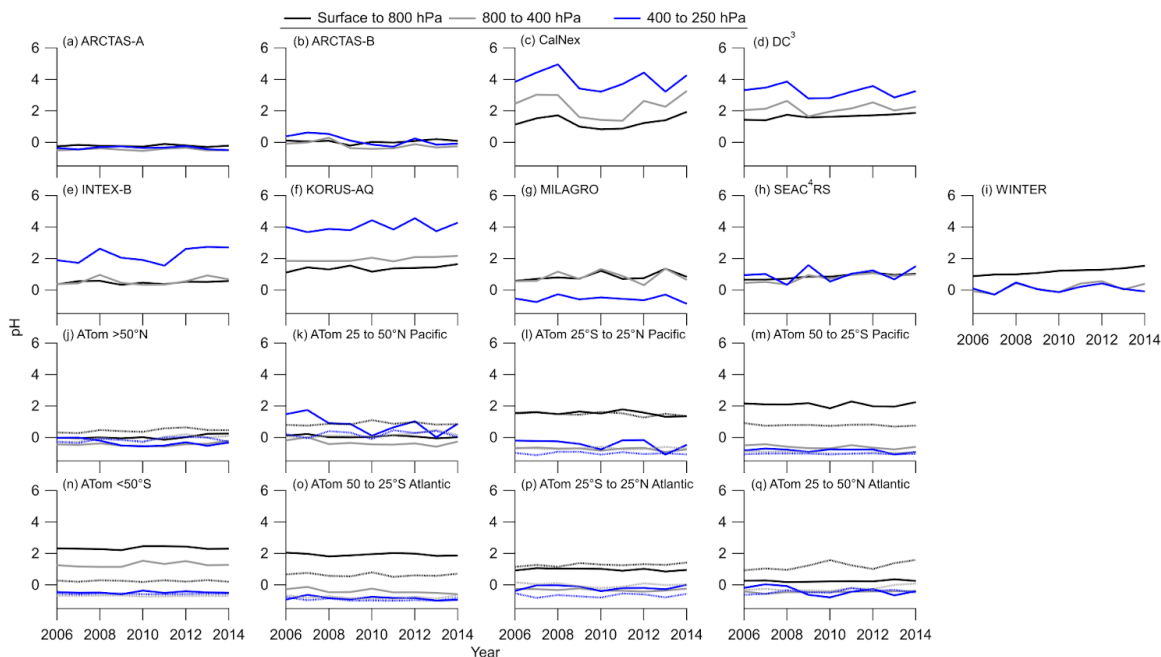
588 *Supplemental Figure 26. Evaluation in the predicted trends of ammonium balance over a*
 589 *decade with meteorology constant. NH_4^+ from GEOS-Chem, from 2006 to 2014, with constant*
 590 *meteorology (2010) but varying emissions, for the three pressure levels in the troposphere*
 591 *(surface to 800 (black), 800 to 400 (grey), and 400 to 250 (blue) hPa), for the regions defined in*
 592 *Supplemental Table 2. For the ATom regions, solid is for ATom-1 and dashed is for ATom-2.*

593



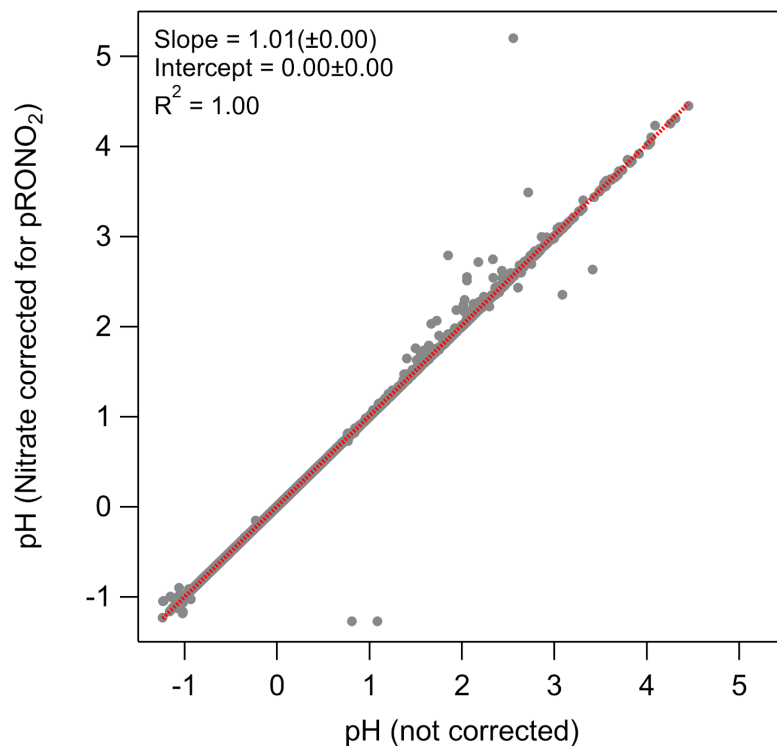
594 *Supplemental Figure 27. Evaluation in the predicted trends of pH over a decade with emissions*
 595 *constant. Same as Supplemental Figure 25. pH, from GEOS-Chem, from 2006 to 2014, with*
 596 *emissions for 2010, for the three pressure levels in the troposphere (surface to 800 (black), 800*
 597 *to 400 (grey), and 400 to 250 (blue) hPa), for the regions defined in Supplemental Table 2. For*
 598 *the ATom regions, solid is for ATom-1 and dashed is for ATom-2.*

599



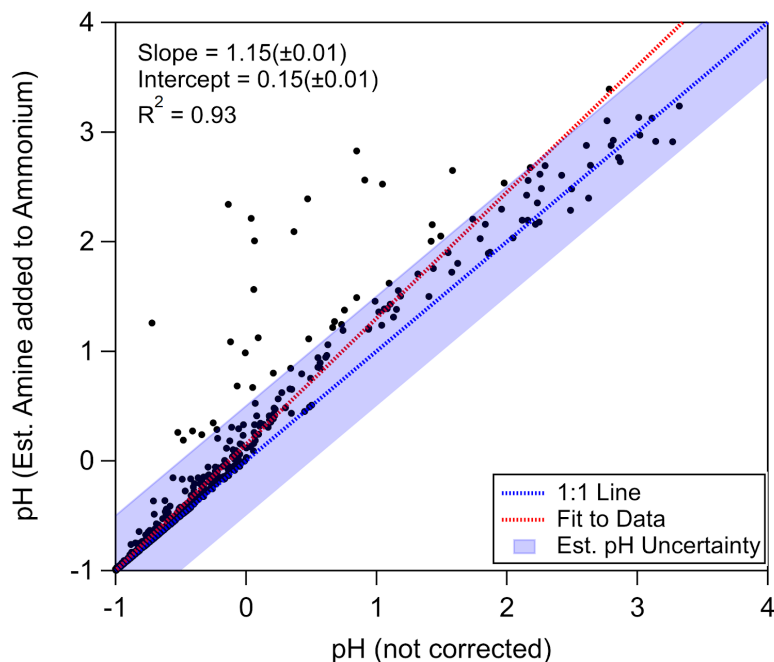
600 *Supplemental Figure 28. Evaluation in the predicted trends of pH over a decade with*
 601 *meteorology constant. Same as Supplemental Figure 26. pH, from GEOS-Chem, from 2006 to*
 602 *2014, with constant meteorology (2010) but varying emissions, for the three pressure levels in*
 603 *the troposphere (surface to 800 (black), 800 to 400 (grey), and 400 to 250 (blue) hPa), for the*
 604 *regions defined in Supplemental Table 2. For the ATom regions, solid is for ATom-1 and dashed*
 605 *is for ATom-2.*

606

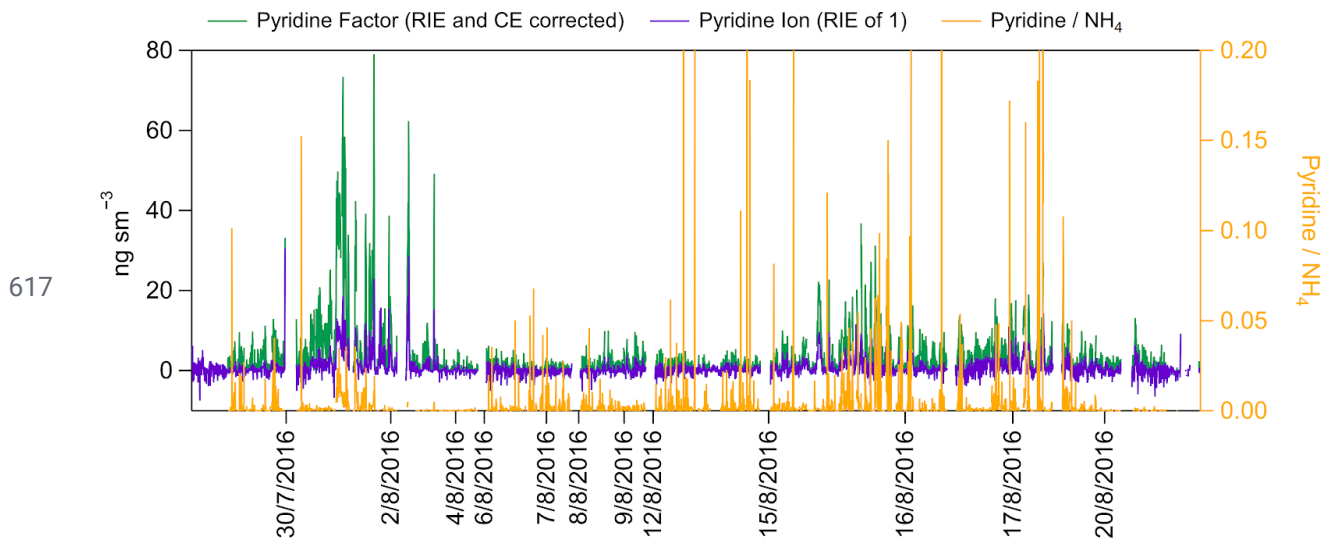


607 *Supplemental Figure 29. Comparison of pH from E-AIM with and without accounting for*
608 *organic nitrate in the mass concentration. Scatter plot of aerosol pH, for SEAC⁴RS, comparing*
609 *pH, where nitrate was corrected for organic oxidized nitrate (pRONO₂, left axis)⁴⁴ versus the pH*
610 *reported here. The regression is ODR and shown in red*

611



612 *Supplemental Figure 30. Comparison of pH from E-AIM with and without accounting for*
613 *reduced organic amines/amides in the mass concentration. Scatter plot of aerosol pH, for*
614 *ATom-2, where ammonium was corrected for estimated amines (left axis) versus the pH reported*
615 *here. The shaded area represents the ± 0.5 pH unit uncertainty estimated from prior studies^{62,63}.*
616 *Blue dashed is the 1:1 line and red dashed is the fit to the data.*



618 *Supplemental Figure 31. Time series of pyridine for during ATom-1. (left) Time series of*
 619 *pyridine, observed by the AMS, during ATom-1, either by the ion ($C_5H_5N^+$, purple) or positive*
 620 *matrix factorization (green)¹⁰⁹. (right) Ratio of the pyridine mass concentration, from the positive*
 621 *matrix factorization result, to the total ammonium mass concentration (orange).*

622 References

- 623 1. Dentener, F. J. & Crutzen, P. J. A three-dimensional model of the global ammonia cycle. *J.*
624 *Atmos. Chem.* **19**, 331–369 (1994).
- 625 2. Kürten, A. *et al.* Experimental particle formation rates spanning tropospheric sulfuric acid
626 and ammonia abundances, ion production rates, and temperatures. *J. Geophys. Res. D:*
627 *Atmos.* **121**, (2016).
- 628 3. Wang, M. *et al.* Rapid growth of new atmospheric particles by nitric acid and ammonia
629 condensation. *Nature* **581**, 184–189 (2020).
- 630 4. Paulot, F. *et al.* Global oceanic emission of ammonia: Constraints from seawater and
631 atmospheric observations. *Global Biogeochem. Cycles* **29**, 1165–1178 (2015).
- 632 5. Williamson, C. J. *et al.* A large source of cloud condensation nuclei from new particle
633 formation in the tropics. *Nature* **574**, 399–403 (2019).
- 634 6. Sutton, M. A. *et al.* Towards a climate-dependent paradigm of ammonia emission and
635 deposition. *Philos. Trans. R. Soc. Lond. B Biol. Sci.* **368**, 20130166 (2013).
- 636 7. Ge, C., Zhu, C., Francisco, J. S., Zeng, X. C. & Wang, J. A molecular perspective for global
637 modeling of upper atmospheric NH₃ from freezing clouds. *Proc. Natl. Acad. Sci. U. S. A.*
638 **115**, 6147–6152 (2018).
- 639 8. Höpfner, M. *et al.* First detection of ammonia (NH₃) in the Asian summer monsoon upper
640 troposphere. *Atmos. Chem. Phys.* **16**, 14357–14369 (2016).
- 641 9. Höpfner, M. *et al.* Ammonium nitrate particles formed in upper troposphere from ground
642 ammonia sources during Asian monsoons. *Nat. Geosci.* **12**, 608–612 (2019).
- 643 10. Wang, J., Jacob, D. J. & Martin, S. T. Sensitivity of sulfate direct climate forcing to the

- 644 hysteresis of particle phase transitions. *J. Geophys. Res.* **113**, 13791 (2008).
- 645 11. Salcedo, D. *et al.* Characterization of ambient aerosols in Mexico City during the
646 MCMA-2003 campaign with Aerosol Mass Spectrometry: results from the CENICA
647 Supersite. *Atmos. Chem. Phys.* **6**, 925–946 (2006).
- 648 12. *CRC Handbook of Chemistry and Physics, 100th Edition, 2019 - 2020*. 1532 (Taylor &
649 Francis Group, 2019).
- 650 13. Heald, C. L. *et al.* Contrasting the direct radiative effect and direct radiative forcing of
651 aerosols. *Atmos. Chem. Phys.* **14**, 5513–5527 (2014).
- 652 14. Murphy, J. G. *et al.* Observational constraints on particle acidity using measurements and
653 modelling of particles and gases. *Faraday Discuss.* **200**, 379–395 (2017).
- 654 15. Guo, H. *et al.* Evaluating the Consistency of All Submicron Aerosol Mass Measurements
655 (Total and Speciated) for the NASA Atmospheric Tomography Aircraft Mission. (May 4 -
656 8, 2020) doi:10.5194/egusphere-egu2020-11863.
- 657 16. Ovadnevaite, J. *et al.* On the effect of wind speed on submicron sea salt mass concentrations
658 and source fluxes. *J. Geophys. Res. D: Atmos.* **117**, 1–11 (2012).
- 659 17. Brock, C. A. *et al.* Aerosol size distributions during the Atmospheric Tomography Mission
660 (ATom): methods, uncertainties, and data products. *Atmos. Meas. Tech.* **12**, 3081–3099
661 (2019).
- 662 18. Kupc, A., Williamson, C., Wagner, N. L., Richardson, M. & Brock, C. A. Modification,
663 calibration, and performance of the Ultra-High Sensitivity Aerosol Spectrometer for particle
664 size distribution and volatility measurements during the Atmospheric Tomography Mission
665 (ATom) airborne campaign. *Atmos. Meas. Tech.* **11**, 369–383 (2018).

- 666 19. Guo, H., Nenes, A. & Weber, R. J. The underappreciated role of nonvolatile cations in
667 aerosol ammonium-sulfate molar ratios. *Atmos. Chem. Phys.* **18**, 17307–17323 (2018).
- 668 20. Guo, H. *et al.* The Importance of Size Ranges in Intercomparison of Aerosol Volume
669 Concentration Measurements: A Case Study for Aerosol Mass Spectrometer in the ATom
670 Mission. *Atmos. Meas. Tech. Discuss.* **In Review**, (2020).
- 671 21. Murphy, D. M. *et al.* The distribution of sea-salt aerosol in the global troposphere. *Atmos.*
672 *Chem. Phys.* **19**, 4903–4104 (2019).
- 673 22. Gaston, C. J., Pratt, K. A., Qin, X. & Prather, K. A. Real-Time detection and mixing state of
674 methanesulfonate in single particles at an inland urban location during a phytoplankton
675 bloom. *Environ. Sci. Technol.* **44**, 1566–1572 (2010).
- 676 23. Gaston, C. J. *et al.* The Cloud Nucleating Properties and Mixing State of Marine Aerosols
677 Sampled along the Southern California Coast. *Atmosphere* **9**, 52 (2018).
- 678 24. Ault, A. P. *et al.* Size-dependent changes in sea spray aerosol composition and properties
679 with different seawater conditions. *Environ. Sci. Technol.* **47**, 5603–5612 (2013).
- 680 25. Palm, B. B. *et al.* In situ secondary organic aerosol formation from ambient pine forest air
681 using an oxidation flow reactor. *Atmos. Chem. Phys.* **16**, 2943–2970 (2016).
- 682 26. Fuchs, N. A. & Sutugin, A. G. High-Dispersed Aerosols. in *Topics in Current Aerosol*
683 *Research* (eds. Hidy, G. M. & Brock, J. R.) (Pergamon, 1971).
- 684 27. Seinfeld, J. H. & Pandis, S. N. *Atmospheric Chemistry and Physics: From Air Pollution to*
685 *Climate Change*. 1232 (John Wiley & Sons, Inc., 2006).
- 686 28. Katich, J. M. *et al.* Strong Contrast in Remote Black Carbon Aerosol Loadings Between the
687 Atlantic and Pacific Basins. *J. Geophys. Res. D: Atmos.* **123**, 151 (2018).

- 688 29. Park, K., Kittelson, D. B., Zachariah, M. R. & McMurry, P. H. Measurement of Inherent
689 Material Density of Nanoparticle Agglomerates. *J. Nanopart. Res.* **6**, 267–272 (2004).
- 690 30. Froyd, K. D. *et al.* A new method to quantify mineral dust and other aerosol species from
691 aircraft platforms using single-particle mass spectrometry. *Atmos. Meas. Tech.* **12**,
692 6209–6239 (2019).
- 693 31. Faloon, I. Sulfur processing in the marine atmospheric boundary layer: A review and
694 critical assessment of modeling uncertainties. *Atmos. Environ.* **43**, 2841–2854 (2009).
- 695 32. Prather, K. A. *et al.* Bringing the ocean into the laboratory to probe the chemical complexity
696 of sea spray aerosol. *Proc. Natl. Acad. Sci. U. S. A.* **110**, 7550–7555 (2013).
- 697 33. Pye, H. O. T. *et al.* Effect of changes in climate and emissions on future
698 sulfate-nitrate-ammonium aerosol levels in the United States. *J. Geophys. Res.* **114**, 1097
699 (2009).
- 700 34. Jaeglé, L., Quinn, P. K., Bates, T. S., Alexander, B. & Lin, J.-T. Global distribution of sea
701 salt aerosols: new constraints from in situ and remote sensing observations. *Atmos. Chem.*
702 *Phys.* **11**, 3137–3157 (2011).
- 703 35. Ordou, N. & Agranovski, I. E. Mass distribution and elemental analysis of the resultant
704 atmospheric aerosol particles generated in controlled biomass burning processes. *Atmos.*
705 *Res.* **198**, 108–112 (2017).
- 706 36. Hodzic, A. *et al.* Characterization of Organic Aerosol across the Global Remote
707 Troposphere: A comparison of ATom measurements and global chemistry models. *Atmos.*
708 *Chem. Phys.* **20**, 4607–4635 (2020).
- 709 37. Lee, A. K. Y. *et al.* Single-particle characterization of biomass burning organic aerosol

- 710 (BBOA): evidence for non-uniform mixing of high molecular weight organics and
711 potassium. *Atmos. Chem. Phys.* **16**, 5561–5572 (2016).
- 712 38. Guo, H. *et al.* Fine particle pH and gas–particle phase partitioning of inorganic species in
713 Pasadena, California, during the 2010 CalNex campaign. *Atmos. Chem. Phys.* **17**,
714 5703–5719 (2017).
- 715 39. Keene, W. C. & Savoie, D. L. The pH of deliquesced sea-salt aerosol in polluted marine air.
716 *Geophys. Res. Lett.* **25**, 2181–2184 (1998).
- 717 40. Keene, W. C., Pszenny, A. A. P., Maben, J. R. & Sander, R. Variation of marine aerosol
718 acidity with particle size. *Geophys. Res. Lett.* **29**, 1101 (2002).
- 719 41. Keene, W. C., Pszenny, A. A. P., Maben, J. R., Stevenson, E. & Wall, A. Closure evaluation
720 of size-resolved aerosol pH in the New England coastal atmosphere during summer. *J.*
721 *Geophys. Res. D: Atmos.* **109**, (2004).
- 722 42. Smith, A. M. *et al.* Ammonia sources, transport, transformation, and deposition in coastal
723 New England during summer. *J. Geophys. Res. D: Atmos.* **112**, (2007).
- 724 43. Farmer, D. K. *et al.* Response of an aerosol mass spectrometer to organonitrates and
725 organosulfates and implications for atmospheric chemistry. *Proc. Natl. Acad. Sci. U. S. A.*
726 **107**, 6670–6675 (2010).
- 727 44. Fry, J. L. *et al.* Observations of gas- and aerosol-phase organic nitrates at
728 BEACHON-RoMBAS 2011. *Atmos. Chem. Phys.* **13**, 8585–8605 (2013).
- 729 45. Huffman, J. a. *et al.* Chemically-resolved aerosol volatility measurements from two
730 megacity field studies. *Atmos. Chem. Phys.* **9**, 7161–7182 (2009).
- 731 46. Chen, Y. *et al.* Response of the Aerodyne Aerosol Mass Spectrometer to Inorganic Sulfates

- 732 and Organosulfur Compounds: Applications in Field and Laboratory Measurements.
733 *Environ. Sci. Technol.* **53**, 5176–5186 (2019).
- 734 47. Kiendler-Scharr, A. *et al.* Ubiquity of organic nitrates from nighttime chemistry in the
735 European submicron aerosol: Organic Nitrates in European PM₁. *Geophys. Res. Lett.* **43**,
736 7735–7744 (2016).
- 737 48. Ng, N. L. *et al.* Nitrate radicals and biogenic volatile organic compounds: oxidation,
738 mechanisms, and organic aerosol. *Atmos. Chem. Phys.* **17**, 2103–2162 (2017).
- 739 49. Finewax, Z., de Gouw, J. A. & Ziemann, P. J. Identification and Quantification of
740 4-Nitrocatechol Formed from OH and NO₃ Radical-Initiated Reactions of Catechol in Air in
741 the Presence of NO_x: Implications for Secondary Organic Aerosol Formation from Biomass
742 Burning. *Environ. Sci. Technol.* **52**, 1981–1989 (2018).
- 743 50. Iinuma, Y., Böge, O., Gräfe, R. & Herrmann, H. Methyl-nitrocatechols: atmospheric tracer
744 compounds for biomass burning secondary organic aerosols. *Environ. Sci. Technol.* **44**,
745 8453–8459 (2010).
- 746 51. Liu, X. *et al.* Airborne measurements of western U.S. wildfire emissions: Comparison with
747 prescribed burning and air quality implications. *J. Geophys. Res. D: Atmos.* **122**, 6108–6129
748 (2017).
- 749 52. Liu, X. *et al.* Agricultural fires in the southeastern U.S. during SEAC⁴RS: Emissions of
750 trace gases and particles and evolution of ozone, reactive nitrogen, and organic aerosol. *J.*
751 *Geophys. Res. D: Atmos.* **121**, 7383–7414 (2016).
- 752 53. Fisher, J. A. *et al.* Organic nitrate chemistry and its implications for nitrogen budgets in an
753 isoprene- and monoterpene-rich atmosphere: Constraints from aircraft (SEAC⁴RS) and

754 ground-based (SOAS) observations in the Southeast US. *Atmos. Chem. Phys.* **16**, (2016).

755 54. Darer, A. I., Cole-Filipiak, N. C., O'Connor, A. E. & Elrod, M. J. Formation and stability of
756 atmospherically relevant isoprene-derived organosulfates and organonitrates. *Environ. Sci.*
757 *Technol.* **45**, 1895–1902 (2011).

758 55. Nault, B. A. *et al.* Secondary Organic Aerosol Production from Local Emissions Dominates
759 the Organic Aerosol Budget over Seoul, South Korea, during KORUS-AQ. *Atmos. Chem.*
760 *Phys.* **18**, 17769–17800 (2018).

761 56. Almeida, J. *et al.* Molecular understanding of sulphuric acid-amine particle nucleation in
762 the atmosphere. *Nature* **502**, 359–363 (2013).

763 57. Ge, X., Shaw, S. L. & Zhang, Q. Toward understanding amines and their degradation
764 products from postcombustion CO₂ capture processes with aerosol mass spectrometry.
765 *Environ. Sci. Technol.* **48**, 5066–5075 (2014).

766 58. Pyridine. *NIST Chemistry WebBook, SRD 69*
767 <https://webbook.nist.gov/cgi/cbook.cgi?ID=C110861&Mask=200#Mass-Spec>.

768 59. Ethanamine, N-ethyl-. *NIST Chemistry WebBook, SRD 69*
769 <https://webbook.nist.gov/cgi/cbook.cgi?ID=C109897&Mask=200#Mass-Spec>.

770 60. Sorooshian, A. *et al.* On the link between ocean biota emissions, aerosol, and maritime
771 clouds: Airborne, ground, and satellite measurements off the coast of California. *Global*
772 *Biogeochem. Cycles* **23**, GB4007 (2009).

773 61. Hodshire, A. L. *et al.* The potential role of methanesulfonic acid (MSA) in aerosol
774 formation and growth and the associated radiative forcings. *Atmos. Chem. Phys.* **19**,
775 3137–3160 (2019).

- 776 62. Guo, H. *et al.* Fine-particle water and pH in the southeastern United States. *Atmos. Chem.*
777 *Phys.* **15**, 5211–5228 (2015).
- 778 63. Battaglia, M. A., Jr., Weber, R. J., Nenes, A. & Hennigan, C. J. Effects of Water-soluble
779 Organic Carbon on Aerosol pH. *Atmos. Chem. Phys. Disc.* 1–36 (2019).
- 780 64. Riva, M. *et al.* Increasing Isoprene Epoxydiol-to-Inorganic Sulfate Aerosol Ratio Results in
781 Extensive Conversion of Inorganic Sulfate to Organosulfur Forms: Implications for Aerosol
782 Physicochemical Properties. *Environ. Sci. Technol.* **53**, 8682–8694 (2019).
- 783 65. Schueneman, M. K. *et al.* Aerosol pH indicator and organosulfate detectability from
784 Aerosol Mass Spectrometry measurements. *Atmos. Meas. Tech. Discuss.* **Accepted**, (2020).
- 785 66. Liao, J. *et al.* Airborne measurements of organosulfates over the continental U.S. *J.*
786 *Geophys. Res. D: Atmos.* **120**, 2990–3005 (2015).
- 787 67. Pye, H. O. T. *et al.* The Acidity of Atmospheric Particles and Clouds. *Atmos. Chem. Phys.*
788 **20**, 4809–4888 (2020).
- 789 68. Guo, H. *et al.* Fine particle pH and the partitioning of nitric acid during winter in the
790 northeastern United States. *J. Geophys. Res. D: Atmos.* **121**, 10,355–10,376 (2016).
- 791 69. Gaston, C. J. *et al.* Reactive Uptake of an Isoprene-Derived Epoxydiol to Submicron
792 Aerosol Particles. (2014) doi:10.1021/es5034266.
- 793 70. Thornton, J. A., Jaeglé, L. & McNeill, V. F. Assessing known pathways for HO₂ loss in
794 aqueous atmospheric aerosols: Regional and global impacts on tropospheric oxidants. *J.*
795 *Geophys. Res. D: Atmos.* **113**, D05303 (2008).
- 796 71. Meskhidze, N., Chameides, W. L., Nenes, A. & Chen, G. Iron mobilization in mineral dust:
797 Can anthropogenic SO₂ emissions affect ocean productivity? *Geophys. Res. Lett.* **30**, 2085

- 798 (2003).
- 799 72. Ackendorf, J. M., Ippolito, M. G. & Galloway, M. M. pH Dependence of the
800 Imidazole-2-carboxaldehyde Hydration Equilibrium: Implications for Atmospheric Light
801 Absorbance. *Environ. Sci. Technol. Lett.* **4**, 551–555 (2017).
- 802 73. Losey, D. J., Ott, E.-J. E. & Freedman, M. A. Effects of High Acidity on Phase Transitions
803 of an Organic Aerosol. *J. Phys. Chem. A* **122**, 3819–3828 (2018).
- 804 74. Molina, L. T. *et al.* An overview of the MILAGRO 2006 Campaign: Mexico City emissions
805 and their transport and transformation. *Atmos. Chem. Phys.* **10**, 8697–8760 (2010).
- 806 75. Singh, H. B., Brune, W. H., Crawford, J. H., Flocke, F. & Jacob, D. J. Chemistry and
807 transport of pollution over the Gulf of Mexico and the Pacific: spring 2006 INTEX-B
808 campaign overview and first results. *Atmos. Chem. Phys.* **9**, 2301–2318 (2009).
- 809 76. Jacob, D. J. *et al.* The Arctic Research of the Composition of the Troposphere from Aircraft
810 and Satellites (ARCTAS) mission: design, execution, and first results. *Atmos. Chem. Phys.*
811 **10**, 5191–5212 (2010).
- 812 77. Ryerson, T. B. *et al.* The 2010 California Research at the Nexus of Air Quality and Climate
813 Change (CalNex) field study. *J. Geophys. Res. D: Atmos.* **118**, 5830–5866 (2013).
- 814 78. Barth, M. C. *et al.* The Deep Convective Clouds and Chemistry (DC3) Field Campaign.
815 *Bull. Am. Meteorol. Soc.* **96**, 1281–1309 (2015).
- 816 79. Toon, O. B. *et al.* Planning, implementation, and scientific goals of the Studies of Emissions
817 and Atmospheric Composition, Clouds and Climate Coupling by Regional Surveys
818 (SEAC⁴RS) field mission. *J. Geophys. Res. D: Atmos.* **121**, 4967–5009 (2016).
- 819 80. Schroder, J. C. *et al.* Sources and Secondary Production of Organic Aerosols in the

- 820 Northeastern US during WINTER. *J. Geophys. Res. D: Atmos.* (2018)
821 doi:10.1029/2018JD028475.
- 822 81. Jordan, C. E. *et al.* Investigation of factors controlling PM_{2.5} variability across the South
823 Korean Peninsula during KORUS-AQ. *Elementa: Science of the Anthropocene* **8**, (2020).
- 824 82. DeCarlo, P. F. *et al.* Field-deployable, high-resolution, time-of-flight aerosol mass
825 spectrometer. *Anal. Chem.* **78**, 8281–8289 (2006).
- 826 83. DeCarlo, P. F. *et al.* Fast airborne aerosol size and chemistry measurements above Mexico
827 City and Central Mexico during the MILAGRO campaign. *Atmos. Chem. Phys.* **8**,
828 4027–4048 (2008).
- 829 84. Crounse, J. D., McKinney, K. A., Kwan, A. J. & Wennberg, P. O. Measurement of
830 Gas-Phase Hydroperoxides by Chemical Ionization Mass Spectrometry. *Anal. Chem.* **78**,
831 6726–6732 (2006).
- 832 85. Dunlea, E. J. *et al.* Evolution of Asian aerosols during transpacific transport in INTEX-B.
833 *Atmos. Chem. Phys.* **9**, 7257–7287 (2009).
- 834 86. Cubison, M. J. *et al.* Effects of aging on organic aerosol from open biomass burning smoke
835 in aircraft and laboratory studies. *Atmos. Chem. Phys.* **11**, 12049–12064 (2011).
- 836 87. Talbot, R. W. *et al.* Large-scale distributions of tropospheric nitric, formic, and acetic acids
837 over the western Pacific basin during wintertime. *J. Geophys. Res.: Atmos.* **102**,
838 28303–28313 (1997).
- 839 88. Drewnick, F. *et al.* A New Time-of-Flight Aerosol Mass Spectrometer
840 (TOF-AMS)—Instrument Description and First Field Deployment. *Aerosol Sci. Technol.* **39**,
841 637–658 (2005).

- 842 89. Bahreini, R. *et al.* Gasoline emissions dominate over diesel in formation of secondary
843 organic aerosol mass. *Geophys. Res. Lett.* **39**, L06805 (2012).
- 844 90. Nowak, J. B. *et al.* Airborne observations of ammonia and ammonium nitrate formation
845 over Houston, Texas. *J. Geophys. Res.* **115**, 2706 (2010).
- 846 91. Neuman, J. A. *et al.* Fast-response airborne in situ measurements of HNO₃ during the Texas
847 2000 Air Quality Study. *J. Geophys. Res.* **107**, 4436 (2002).
- 848 92. Lee, B. H. *et al.* An Iodide-Adduct High-Resolution Time-of-Flight Chemical-Ionization
849 Mass Spectrometer: Application to Atmospheric Inorganic and Organic Compounds.
850 *Environ. Sci. Technol.* **48**, 6309–6317 (2014).
- 851 93. Tsigaridis, K. *et al.* The AeroCom evaluation and intercomparison of organic aerosol in
852 global models. *Atmos. Chem. Phys.* **14**, 10845–10895 (2014).
- 853 94. Marais, E. A. *et al.* Aqueous-phase mechanism for secondary organic aerosol formation
854 from isoprene: application to the southeast United States and co-benefit of SO₂ emission
855 controls. *Atmos. Chem. Phys.* **16**, 1603–1618 (2016).
- 856 95. Jo, D. S. *et al.* A simplified parameterization of isoprene-epoxydiol-derived secondary
857 organic aerosol (IEPOX-SOA) for global chemistry and climate models: a case study with
858 GEOS-Chem v11-02-rc. *Geosci. Model Dev.* **12**, 2983–3000 (2019).
- 859 96. Bian, H. *et al.* Investigation of global particulate nitrate from the AeroCom phase III
860 experiment. *Atmos. Chem. Phys.* **17**, 12911–12940 (2017).
- 861 97. Kodros, J. K. & Pierce, J. R. Important global and regional differences in aerosol
862 cloud-albedo effect estimates between simulations with and without prognostic aerosol
863 microphysics. *J. Geophys. Res. D: Atmos.* **122**, 4003–4018 (2017).

- 864 98. Horowitz, L. W. *et al.* The GFDL Global Atmospheric Chemistry-Climate Model AM4.1:
865 Model Description and Simulation Characteristics. *J. Adv. Model. Earth Syst.* (2020)
866 doi:10.1029/2019MS002032.
- 867 99. Müller, C. *et al.* Seasonal variation of aliphatic amines in marine sub-micrometer particles
868 at the Cape Verde islands. *Atmos. Chem. Phys.* **9**, 9587–9597 (2009).
- 869 100. van Pinxteren, M. *et al.* Chemical characterization of sub-micrometer aerosol particles in
870 the tropical Atlantic Ocean: marine and biomass burning influences. *J. Atmos. Chem.* **72**,
871 105–125 (2015).
- 872 101. Frossard, A. A. *et al.* Sources and composition of submicron organic mass in marine aerosol
873 particles: Marine Aerosol Organic Mass Composition. *J. Geophys. Res. D: Atmos.* **119**,
874 12,977–13,003 (2014).
- 875 102. Youn, J.-S., Crosbie, E., Maudlin, L. C., Wang, Z. & Sorooshian, A. Dimethylamine as a
876 major alkyl amine species in particles and cloud water: Observations in semi-arid and
877 coastal regions. *Atmos. Environ.* **122**, 250–258 (2015).
- 878 103. Gibb, S. W., Mantoura, R. F. C. & Liss, P. S. Ocean-atmosphere exchange and atmospheric
879 speciation of ammonia and methylamines in the region of the NW Arabian Sea. *Global*
880 *Biogeochem. Cycles* **13**, 161–178 (1999).
- 881 104. Facchini, M. C. *et al.* Important source of marine secondary organic aerosol from biogenic
882 amines. *Environ. Sci. Technol.* **42**, 9116–9121 (2008).
- 883 105. Huang, S. *et al.* Source apportionment of the organic aerosol over the Atlantic Ocean from
884 53°N to 53°S: significant contributions from marine emissions and long-range transport.
885 *Atmos. Chem. Phys.* **18**, 18043–18062 (2018).

- 886 106. Blake, N. J. *et al.* The seasonal evolution of NMHC's and light alkyl nitrates at middle to
887 northern latitudes during TOPSE. *J. Geophys. Res. D: Atmos.* **108**, 8359 (2003).
- 888 107. Dibb, J. E. *et al.* Airborne sampling of aerosol particles: Comparison between surface
889 sampling at Christmas Island and P-3 sampling during PEM-Tropics B. *J. Geophys. Res.*
890 **108**, 8230 (2002).
- 891 108. Dibb, J. E. *et al.* Aerosol chemical composition in Asian continental outflow during the
892 TRACE-P campaign: Comparison with PEM-West B. *J. Geophys. Res.: Atmos.* **108**, 8815
893 (2003).
- 894 109. Ulbrich, I. M., Canagaratna, M. R., Zhang, Q., Worsnop, D. R. & Jimenez, J. L.
895 Interpretation of organic components from Positive Matrix Factorization of aerosol mass
896 spectrometric data. *Atmos. Chem. Phys.* **9**, 2891–2918 (2009).

897